

# Active Seismic Refraction, Reflection and Surface-Wave Surveys in Thick Debris-Covered Glacial Environments

Tyler Kuehn<sup>1</sup>, John W Holt<sup>1,2</sup>, Roy Johnson<sup>1</sup>, and Tyler Meng<sup>2</sup>

<sup>1</sup>Department of Geosciences, University of Arizona

<sup>2</sup>Arizona Lunar and Planetary Laboratory, University

October 27, 2023

## Abstract

Debris-covered glaciers and rock glaciers have been increasingly studied in recent years because of the role they play within local watersheds, glacial ablation models due to climate change, and as analogs for buried ice features on planetary bodies such as Mars. Characterizing the supraglacial debris layer is a large part of these efforts. Geophysical exploration of debris-covered glaciers has mostly excluded active seismic methods, with the exception of refraction studies, due to the attenuating properties of the debris cover and field survey efficiency. We evaluate the accuracy, field efficiency, and effectiveness of seismic refraction, reflection, and surface-wave surveys for determining the elastic properties of the debris layer and any underlying layers on debris-covered glaciers using sites from Sourdough Rock Glacier and in the Malaspina Glacier forelands in Southcentral Alaska. We compare our seismic results with our results from ground-penetrating radar. Our results indicate that the interface between the debris layer and the ice can be imaged using seismic reflection methods, and that multi-channel analysis of surface waves (MASW) can provide insight to the variability of the shear-wave structure within the debris layer. We image an ultra-shallow seismic reflection from the bottom of the loose debris layer using ultra-dense receiver arrays. This study also presents results using multi-channel analysis of surface waves (MASW) on a debris-covered glacier, which we find could be a valuable addition to the toolbox of future geophysical investigations on these landforms.

1  
2  
3  
4  
5  
6  
7  
8  
9  
10  
11  
12  
13  
14  
15  
16  
17  
18  
19  
20  
21  
22  
23  
24  
25  
26  
27

# Active Seismic Refraction, Reflection and Surface-Wave Surveys in Thick Debris-Covered Glacial Environments

Tyler Kuehn<sup>1</sup>, John W. Holt<sup>1,2</sup>, Roy Johnson<sup>1</sup>, Tyler Meng<sup>2</sup>

<sup>1</sup>University of Arizona Department of Geosciences

<sup>2</sup>University of Arizona Lunar and Planetary Laboratory

Corresponding author: Tyler Kuehn ([tkuehn@arizona.edu](mailto:tkuehn@arizona.edu))

## Key Points:

- We use ultra-dense receiver spacing to image seismic reflections from the loose debris layer on a debris-covered glacier for the first time.
- We demonstrate we can obtain shear-wave velocity structure (stiffness) observations for debris cover on glaciers.

## 28 **Abstract**

29 Debris-covered glaciers and rock glaciers have been increasingly studied in recent years  
30 because of the role they play within local watersheds, glacial ablation models due to climate  
31 change, and as analogs for buried ice features on planetary bodies such as Mars. Characterizing  
32 the supraglacial debris layer is a large part of these efforts. Geophysical exploration of debris-  
33 covered glaciers has mostly excluded active seismic methods, with the exception of refraction  
34 studies, due to the attenuating properties of the debris cover and field survey efficiency. We  
35 evaluate the accuracy, field efficiency, and effectiveness of seismic refraction, reflection, and  
36 surface-wave surveys for determining the elastic properties of the debris layer and any underlying  
37 layers on debris-covered glaciers using sites from Sourdough Rock Glacier and in the Malaspina  
38 Glacier forelands in Southcentral Alaska. We compare our seismic results with our results from  
39 ground-penetrating radar. Our results indicate that the interface between the debris layer and the  
40 ice can be imaged using seismic reflection methods, and that multi-channel analysis of surface  
41 waves (MASW) can provide insight to the variability of the shear-wave structure within the debris  
42 layer. We image an ultra-shallow seismic reflection from the bottom of the loose debris layer using  
43 ultra-dense receiver arrays. This study also presents results using multi-channel analysis of surface  
44 waves (MASW) on a debris-covered glacier, which we find could be a valuable addition to the  
45 toolbox of future geophysical investigations on these landforms.

## 46 **Plain Language Summary**

47 Debris-covered glaciers and rock glaciers are glaciers with a loose rock layer covering all  
48 or most of their surface. This layer can be several meters thick and plays an important role in how  
49 fast the glacier melts. These types of glaciers are an important analog to similar buried ice features  
50 we observe on other planetary bodies, such as Mars. Typically, the subsurface of these glaciers is  
51 studied using the geophysical method of ground-penetrating radar, though in this paper we explore  
52 how active-source seismic methods could be utilized in future surveys. We demonstrate that using  
53 active-seismic techniques can provide information on the ‘stiffness’ of the debris layer, which can  
54 add context to a ground-penetrating radar survey and ultimately aid in interpreting glacial features.

## 55 **1 Introduction1.1 Background and Motivation**

56 Debris-covered glaciers (DCG) are unique geomorphological landforms that can be found  
57 across the globe anywhere clean-surfaced glaciers are formed, in high mountain environments  
58 where there is an abundant supply of rockfall debris. They are characterized by a surficial debris  
59 cover that varies in thickness spanning the accumulation zone to the glacier terminus. The debris  
60 layer acts as insulation for the subsurface ice, decreasing the ablation rate with increasing debris  
61 thickness (Östrem, 1959; see also Nicholson & Benn, 2006). The factors that contribute to the  
62 evolution of the debris surface and the physical properties within the debris are being increasingly  
63 studied in recent years to better understand the response of DCG to climate change (Rowan et al.,  
64 2015; Scherler et al., 2011; Yde & Paasche, 2010) and the effects on local watersheds, glacial  
65 hazards and landscape evolution.

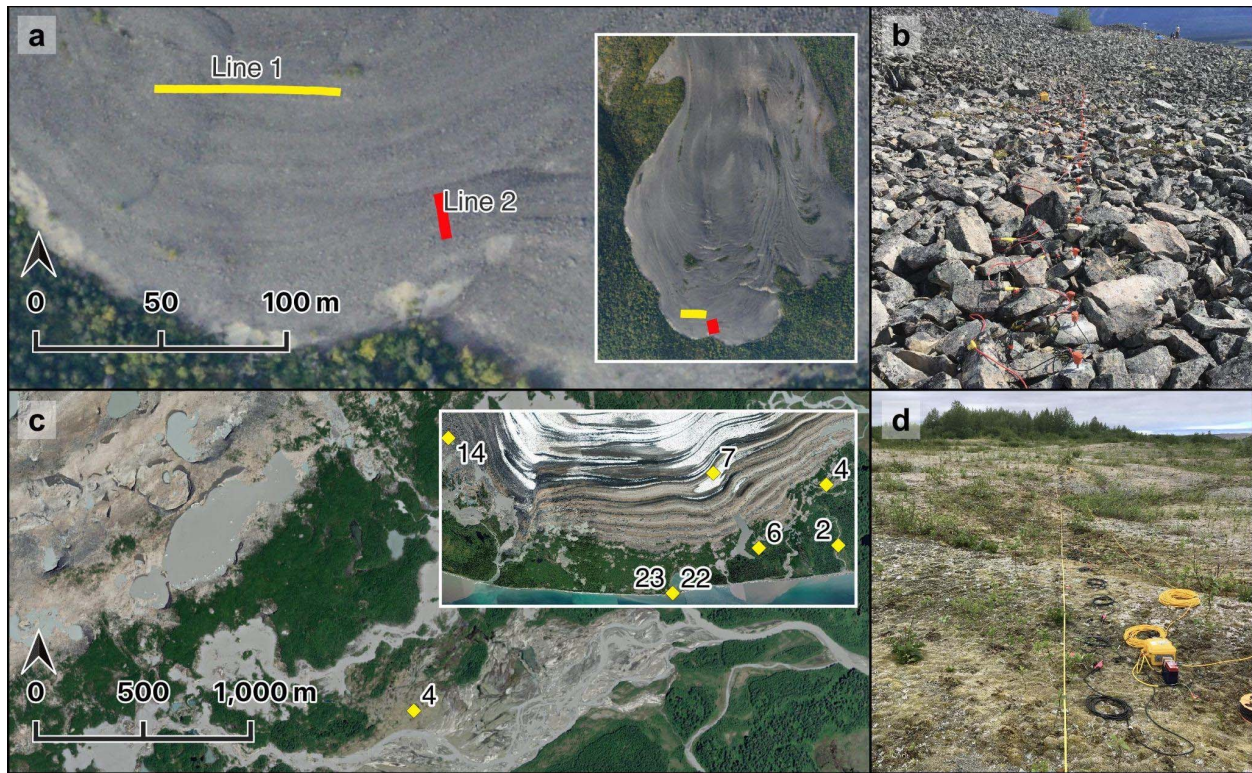
66 In addition to these terrestrial applications, DCG have important planetary exploration  
67 implications for similar features observed on Mars (Head et al., 2010; Holt et al., 2008; Levy et  
68 al., 2014). Using DCG on Mars as a potential water resource for future exploration efforts and  
69 human habitation missions has been a recent topic in the planetary exploration community (Abbud-  
70 Madrid et al., 2016). Thickness of the debris layer, clast size distribution, and presence of ice-  
71 cemented debris are important parameters affecting the feasibility of in-situ resource utilization  
72 that need to be accurately constrained in future planetary exploration studies.

73 Remote alpine environments and rugged terrain make exploration of debris-covered  
74 glaciers on Earth by drilling methods prohibitive in both cost and logistics to be widely used. For  
75 that reason, studies of the debris layer and internal structure of DCG have mostly relied on remote  
76 sensing data and geophysical exploration (Bhardwaj et al., 2014; Merz et al., 2016; Paul et al.,  
77 2004). Among the suite of geophysical tools to study DCG, ground-penetrating radar (GPR) has  
78 been the most widely employed method for debris layer thickness investigations (e.g. Florentine  
79 et al., 2014; Petersen et al., 2020), because of the ease of use in rugged field settings and capability  
80 of imaging subsurface glacial structure. In contrast, active seismic exploration methods have not  
81 been widely used on DCG with thick debris cover largely because of field efficiency issues and  
82 signal-to-noise ratios affected by the highly attenuating debris layer. Active-source seismic studies  
83 have been limited to ( $p$ )-wave refraction profiles and seismic refraction tomography (SRT), which  
84 have been shown to accurately delineate zones of pure ice from debris in ice-cored moraines and  
85 debris-covered glaciers (Croce & Milana, 2002; Langston et al., 2011; Musil et al., 2002; Potter,  
86 1972) and have been combined with electrical resistivity methods (Pavoni, 2023; Wagner et al.,  
87 2019). Attempts at seismic reflection studies on rock glaciers have not been as successful (Maurer  
88 & Hauck, 2007; Musil et al., 2002). The intent of this study is to apply and evaluate seismic  
89 reflection and active-source multi-channel analysis of surface waves (MASW) to quantify the  
90 thickness and elastic properties of the debris layer on rock glaciers. If appropriate acquisition  
91 parameters are followed, the dataset for these surveys can be collected at the same time, and can  
92 also be used to pick the first-arrival times for the refraction and reflection dataset. To determine  
93 the effectiveness and accuracy of these methods, we compare the results of ground-penetrating  
94 radar (GPR) profiles taken on coincident lines, synthetic seismic shot records using a finite-  
95 difference wave propagation modeler, and the active seismic results from two glacial study sites.  
96 We use results from refraction tomography profiles to inform ( $p$ )-wave *a priori* values used in the  
97 reflection forward modeling and surface-wave inversion process.

## 98 1.2 Overview of Study Areas

99  
100 Sourdough Rock Glacier is located in the Wrangell mountains near McCarthy, Alaska.  
101 Previous GPR surveys have confirmed that the glacier features a debris layer approximately 2.5 to  
102 3 meters thick overlying an ice-rich core that extends up to 50 meters in depth (Meng et al., 2022;  
103 Petersen et al., 2016).

104 We compare active-source surface-wave acquisition parameters, processing methods, and  
105 results from Sourdough to those from a second site in the Malaspina Glacier forelands, located in  
106 Wrangell-St. Elias National Park. Malaspina Glacier is a widely studied large piedmont-style  
107 glacier in the Saint Elias mountains near Yakutat, Alaska (Russell, 1893; Sauber et al., 2005). The  
108 glacier is protected from tidal influences by a thin strip of land composed of glacial outwash  
109 deposits known as the Malaspina forelands. In certain parts of the forelands, sediments overlie  
110 large continuous masses of remnant glacial ice emplaced by past glacial activity (Gustavson &  
111 Boothroyd, 1987). This remnant ice is the target of our surveys. The active seismic data presented  
112 here was collected in the summer of 2021 at several sites as part of a larger ongoing study to  
113 quantify the spatial distribution of buried ground ice in the forelands.  
114

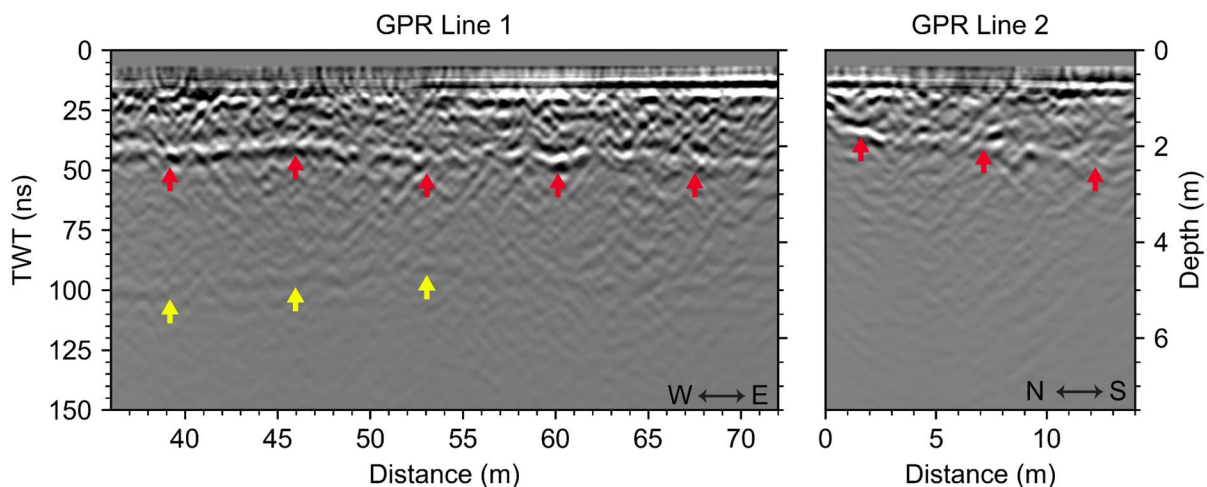


115  
116 **Figure 1.** a) Seismic line locations near the terminus of Sourdough Rock Glacier and inlay map  
117 for full glacier context. b) Field photo of typical terrain on Sourdough Rock Glacier with  
118 geophones ground-coupled for line 1 at 0.5-meter intervals. c) Aerial image of Site 4 in the  
119 Malaspina forelands showing nearby thermokarst activity with inlay map of all sites where active  
120 seismic data was collected across the forelands. d) Field photo of the terrain at Site 4 with  
121 geophones inserted into the ground at 1-meter intervals.

### 122 1.3 Ground-Penetrating Radar Context

123  
124 For a baseline comparison with the active seismic methods, we collected ground-  
125 penetrating radar (GPR) profiles along the active seismic lines on Sourdough using a Sensors &

126 Software PulseEKKO Ultra system operated with 200-MHz antennas. The antenna spacing was  
127 0.5 m and traces recording received power as a function of time were collected at discrete 0.1-m  
128 intervals along the profile, allowing for the detection of the radio echo from the dielectric contrast  
129 between the debris and the ice. Using Sensors & Software EKKO\_Project software, we subtracted  
130 the background average, migrated the data, and applied a depth correction assuming a velocity of  
131 0.1 m/ns, which corresponds to a dielectric permittivity of nine. This value is consistent with debris  
132 values from GPR studies on other DCG (Meng et al.; 2022; Monnier & Kinnard, 2013; Petersen  
133 et al., 2020) and it provides a lower bound on estimated debris thickness because most lithologies  
134 do not have a dielectric permittivity exceeding nine (Campbell & Ulrichs, 1969). By picking the  
135 first break of the reflection interpreted to be the debris/ice interface, we find a minimum debris  
136 thickness of 1.5 m and a maximum debris thickness of 2.2 m along these transects (Figure 2). The  
137 uncertainty in the dielectric permittivity of the debris is the largest source of uncertainty in the  
138 GPR-derived debris thickness measurements. Due to environmental conditions and logistical  
139 constraints at the Malaspina survey sites, no GPR data were collected.  
140



141  
142 **Figure 2.** Surface-flattened reflection results from the 200 MHz GPR surveys coincidental with  
143 the seismic line locations. The reflection surface denoted by the red arrows is interpreted as the  
144 bottom of the loose debris layer. A second reflector likely from internal debris in Line 1 around 5  
145 meters depth from 36 to 53 meters distance is marked by the yellow arrows.

#### 146 1.4 Survey Method Background

147  
148 Seismic Refraction is a well-established tool in geophysical investigations for glaciology,  
149 where the start of the seismic signal, termed the (*p*)-wave first arrivals, are picked from the trace  
150 data. The result of the picking process is a set of times (*T*), usually in ms, and offsets from the  
151 source location distance (*X*), usually in m. The *T*-*X* information can then be inverted for (*p*)-wave  
152 structure of the subsurface, and is useful for locating features such as bedrock, geological layer  
153 interfaces, or the water table. The depth of investigation depends on the velocity of the subsurface

154 strata, the length of the seismic array, energy of the source, and attenuation properties of the  
155 materials (Musgrave, 1967).

156 Seismic reflection is a widely used method in oil and gas exploration and has also been  
157 used in glacial studies to determine glacier thickness and internal geometry (e.g. Baker et al.,  
158 2003). Reflections from the layer interfaces are returned to the receiver array as a hyperbolic event,  
159 due to a phenomenon called normal moveout (NMO). The NMO velocity can be solved for by  
160 using the intercept time at zero offset and the geometry of the array (Dix, 1955). The records can  
161 then be corrected using the NMO for each reflection hyperbola event and stacked at a common  
162 depth point (CDP) to create an image of the subsurface layers (Sheriff & Geldart, 1982; Yilmaz,  
163 2001).

164 Multi-channel analysis of surface waves (MASW) is a seismic exploration technique  
165 commonly used in civil engineering site characterizations. It is a useful tool to determine the (*s*)-  
166 wave properties of the geology in the upper tens of meters of the subsurface when using an active  
167 source and dense receiver spacing (Park et al., 1999, 2007). The method takes advantage of the  
168 dispersive properties of Rayleigh waves, the main component of ground roll (Richart, F.E. et al.,  
169 1970). The phase velocities at each frequency component of the Rayleigh waves can be used to  
170 yield a dispersion curve, which is inverted for a shear (*s*)-wave velocity profile of the subsurface  
171 (Park et al., 1999). In typical seismic refraction and reflection shot records, ground roll resulting  
172 from the source can be seen as a distinct cone-shaped event propagating out from the source  
173 location. Ground roll is often unwanted and filtered out of the record to identify other events of  
174 interest such as reflections (Karlı & Bayrak, 2004; Yilmaz, 2001), but MASW acquisition  
175 parameters seek to enhance the ground roll. Since Rayleigh waves can be generated using a  
176 compressive source typically used for (*p*)-wave surveys, seismic refraction, reflection and MASW  
177 surveys can use the same dataset, given that the time of the shot records is long enough to capture  
178 the whole ground-roll package at the farthest offset. The analysis assumes the wavefront is  
179 propagating as a plane wave, so the source must be offset at a far enough distance from the first  
180 receiver to approximate the needed wavefront characteristics. High-frequency surface waves are  
181 also easily attenuated so a maximum offset depending on site characteristics needs to be chosen as  
182 well (Park et al., 1999).

183

## 184 **2 Data Acquisition**

185 At the Malaspina Glacier foreland study sites, the active seismic surveys were optimized  
186 for refraction tomography (SRT) and MASW data collection. 24-channel Geometrics Geode  
187 exploration seismographs were used to connect linear arrays of 24 to 48 geophones at 1-meter  
188 receiver spacing intervals depending on the spatial limitations of the site. We used 4.5-Hz  
189 geophones, a standard frequency to collect active source surface-wave data (Foti et al., 2018; Park  
190 et al., 2002). A 7.25-kg (16-lb) sledgehammer was struck on a 1.9 cm (¾ inch) thick steel plate as  
191 the source. The source was not placed at every receiver station along the transect to collect a  
192 reflection profile due to timing and logistical constraints.

193 On Sourdough Rock Glacier, two 24-channel Geometrics Geode seismographs using 40-  
194 Hz geophones were connected to create 48-channel linear arrays. The active seismic survey lines  
195 were chosen near the terminus of the glacier, over relatively flat areas of the debris surface. Line  
196 1 is oriented roughly east-west with spacing of 0.5 meters. Five overlapping sub-arrays of lengths  
197 of 24 meters created a total transect length of 72 meters. Line 2 is oriented roughly north-south  
198 with a total of 48 receiver stations spaced 0.3-meters apart that span a total distance of 14.4 meters  
199 (Figure 1). We used a recording sampling rate of 0.063 ms. At line 1, five shots were repeated at  
200 each source point to enhance the signal to noise ratio. For line 2, 10 shots per source point were  
201 collected.

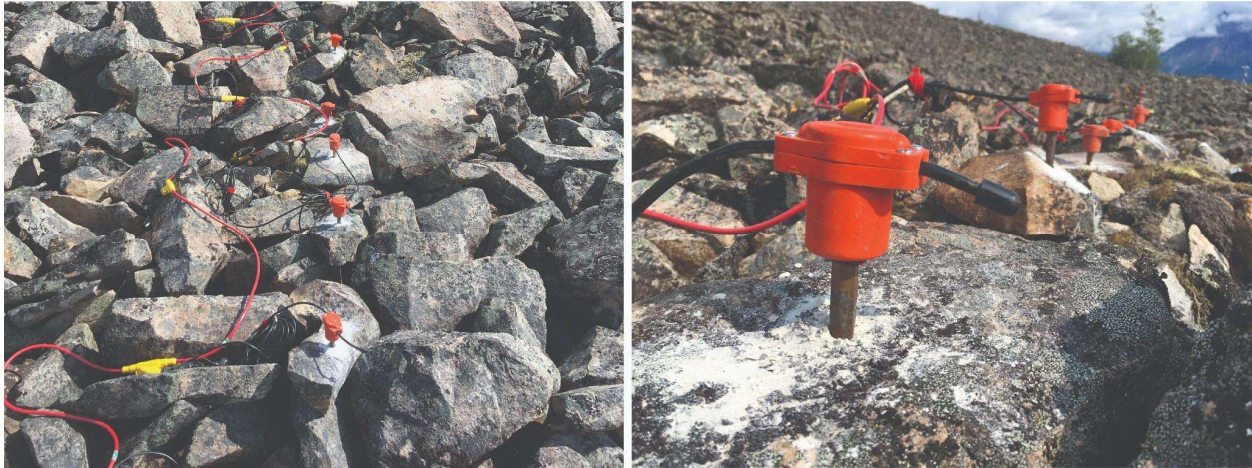
202 The purpose of using higher frequency geophones on Sourdough was primarily to collect  
203 shallow reflection data at high frequencies (Brabham et al., 2005; Steeples et al., 1997), though we  
204 also use the dataset for MASW. A study by Park (2002) detailed the use of higher-frequency  
205 geophones for MASW and found that a reliable dispersion curve was still attainable and the  
206 receivers were able to record at frequencies lower than 10 Hz, though it does limit the investigation  
207 depth depending on site characteristics. Since the aim of our surface-wave study was the upper  
208 few meters of the subsurface, we found this acceptable in order to simultaneously carry out a  
209 reflection survey.

210 A 7.25 kg (16-lb) sledgehammer and a standard 0.63 kg (22 oz) geologist's rock hammer  
211 were used as sources during acquisition. The varying shape and size of the surface debris on  
212 Sourdough ruled out the possibility of using a steel plate as an impact surface for the source  
213 because of inadequate coupling, resulting in the plate bouncing after being struck. Since using an  
214 impact surface was not possible, the source was struck directly on debris-clasts at each shot point.  
215 Most of the surface rocks are loose and platy, which resulted in debris movement, breakage, and  
216 flyrock after sledgehammer strikes, producing unwanted events in shot records. During  
217 acquisition, shot records with obvious effects from these events were not kept after visual  
218 inspection.

219 After some time in the field, it became evident that shots recorded with the rock-hammer  
220 source yielded better field efficiency, less source-generated noise, and more shots could be stacked  
221 at a particular shot location. For those reasons, only the rock hammer was used for reflection  
222 acquisition on the last half of Line 1 and the whole of Line 2, with shot locations at every receiver  
223 station. The heavy sledgehammer was then used at either end of the arrays to generate forward and  
224 reverse shots used for MASW, because the observed surface-waves were stronger than those  
225 generated by the rock hammer.

226 To couple the receivers to the debris surface, geophones with spikes were placed in 0.95  
227 cm ( $\frac{3}{8}$  inch) diameter holes that were drilled into debris clasts using a cordless hammer drill  
228 (Figure 3). This method of coupling was chosen because it allowed for precise positioning of  
229 geophones on the survey line and allowed for the minimization of geophone tilt (Maurer & Hauck,  
230 2007). Each receiver was geo-located using a multi-band RTK GNSS receiver with centimeter  
231 precision at the top of the geophone. The approximate height each geophone sits above the surface,

232 9 cm, was subtracted from the elevation values at each station to infer a topography profile for the  
233 top of the debris layer.  
234



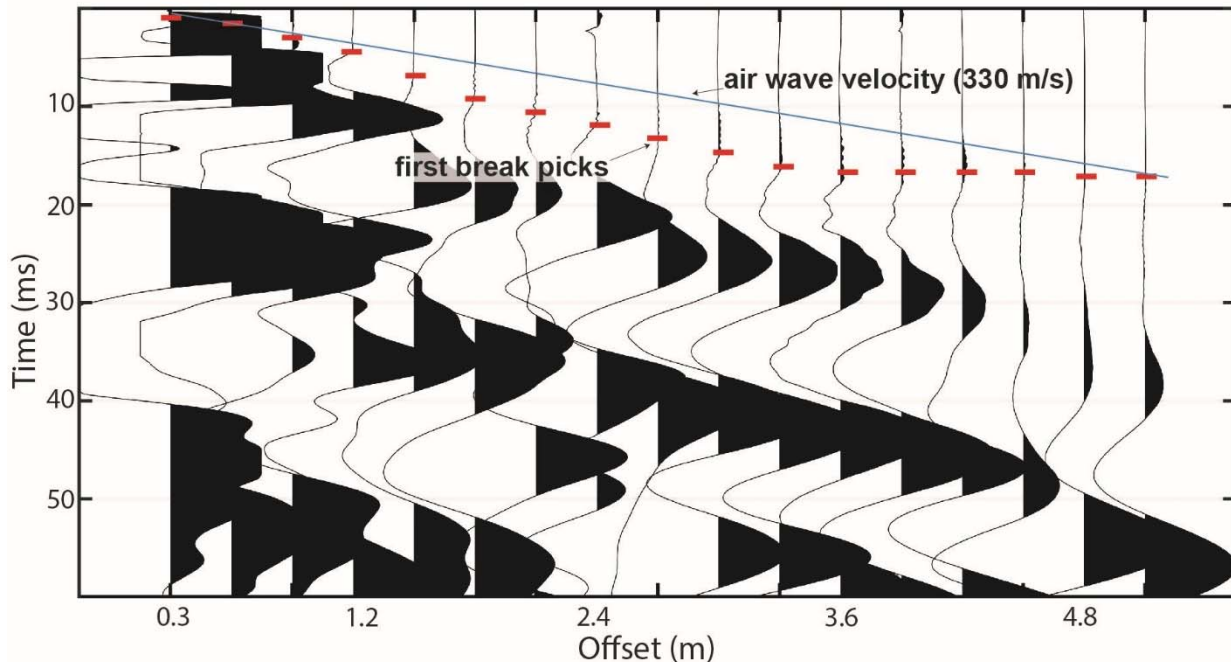
235  
236 **Figure 3.** Method for geophone coupling to individual debris clasts after Maurer & Hauck (2007).

### 237 **3 Processing & Results**

#### 238 **3.1 Refraction Tomography**

239  
240 To pick the first arrival times, we normalize the shot traces and manually pick the data.  
241 The first arrival times for the Malaspina sites were easily identifiable and required no filtering to  
242 pick other than gain-setting manipulation. In the Sourdough records however, the p-wave first  
243 arrivals (the seismic wave traveling along the surface of the debris) is obscured by the air wave  
244 (sound of the hammer hitting the surface) at short offsets (0-5 m) (Figure 4). In these records, the  
245 airwave has a much higher frequency content and lower amplitude than the first arrivals, so the  
246 two can be distinguished to pick a reliable first arrival time for the debris layer. The Sourdough  
247 records are also associated with more source-generated noise, so traces and records that could not  
248 be reliably picked were avoided and clean records were used for the tomography inversion.

249  
250



251 **Figure 4.** An example shot record from Sourdough Line 2 for near-offset receivers. The  
 252 first arrival p-wave (red dashes) is obscured by the air-wave which is represented by the line having  
 253 a slope of 330 m/s and recognized by high-frequency low-amplitude arrivals.  
 254

255  
 256 To invert the refraction data, we use the python Geophysical Inversion Modeling Library  
 257 (pyGIMLi) (Rücker et al., 2017) which uses a shortest-path algorithm (Heincke et al., 2010;  
 258 Ronczka et al., 2017) to calculate seismic energy as ray paths from the modeled velocity structure.  
 259 The inversion scheme requires a data weight for each travel-time pick, which we assign as a linear  
 260 function based on source-receiver offset used in other shallow refraction tomography studies,  
 261 where error increases with offset (Flinchum et al., 2022).

262 We assign a minimum picking error for the Malaspina foreland records of 0.5 ms and a  
 263 maximum error of 2 ms. The Sourdough shot records have a much lower signal-to-noise ratio, so  
 264 we assign a minimum picking error of 1 ms and a maximum of 3 ms. The values of these errors  
 265 were assigned based on standard deviation from the mean pick time of a representative shot record  
 266 for close and far offsets.

267 Tomography results from the refraction first breaks at sites 2, 6, 14, 22 and 23 in the  
 268 Malaspina forelands do not indicate any shallowly buried remnant glacial ice, which has a typical  
 269 ( $p$ )-wave velocity range of 3600-4000 m/s (Baker et al., 2003; Press, 1966) when free of any  
 270 entrained debris. These sites indicate slow velocities (100-800 m/s) in the upper few meters and  
 271 maximum velocities around 2000-2800 m/s. The slower range is consistent with observed  
 272 velocities for dry or well-drained sediments or gravels and the upper range with saturated and more  
 273 consolidated sediments and tills (Press, 1966; Uyanık, 2011). Tomography sections for these sites  
 274 and their corresponding inversion statistics can be found in Appendix A. We do observe a large

275 velocity contrast around 14 meters in depth at Malaspina Site 4 (Figure 5), which we use as a  
276 comparison to the Sourdough sections as this velocity contrast is consistent with expectations for  
277 glacial till over massive ice.

278 The inversion results for Malaspina Site 4 (figure 5) achieve a  $\chi^2$  value of 0.489 and an  
279 RMS of 1.243ms after 15 iterations.  $\chi^2$  is a statistical measure of the observed and expected values  
280 and RMS or root mean square is the standard deviation. Materials with (*p*)-wave values in the  
281 accepted ice-velocity range are observed around 14 meters in depth. Depth to bedrock in the  
282 Malaspina forelands has been previously estimated to be in excess of 150 m (Allen & Smith, 1953),  
283 strongly ruling out the likelihood of a bedrock refraction in the upper 20 m and strengthening the  
284 case for massive remnant glacial ice. The tomography results show higher velocities than typical  
285 massive glacial ice (>4000 m/s) at the bottom of the mesh. It should be noted that the modeled ray  
286 coverage density is not as populated as the top and middle of the mesh, which makes us less certain  
287 of the results. We interpret the overlying strata of debris at this site to range from dry, well-drained  
288 gravel near the surface, to more consolidated wet sands and clays starting at 5-m depth.

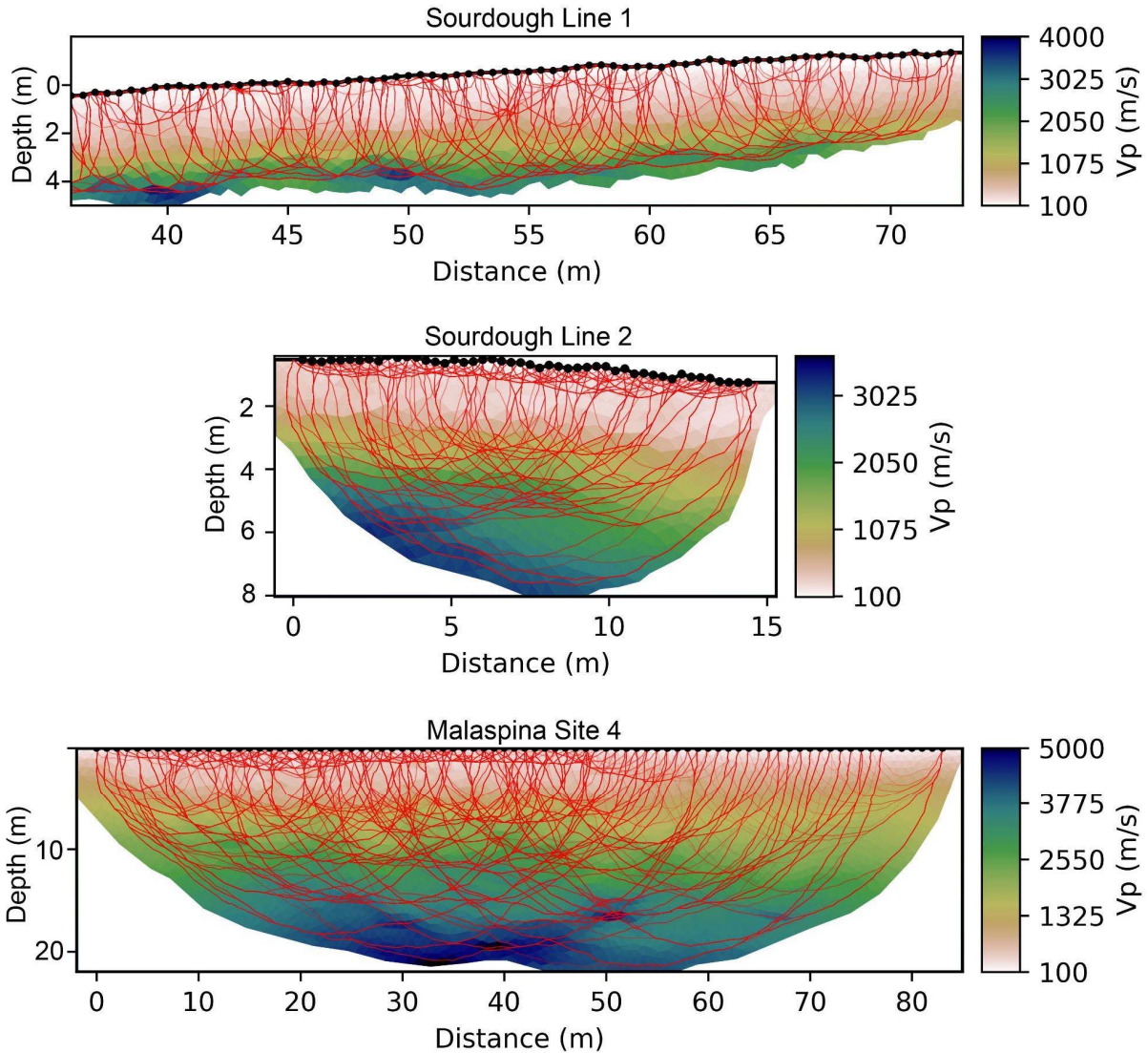
289 For the Sourdough lines, after 15 iterations we achieve a  $\chi^2$  value of 1.12 and an  
290 RMS of 1.02 ms for line 1 and a  $\chi^2$  value of 0.469 and an RMS of 1.848 ms for line 2 (Figure 5).  
291 The loose debris layer ranging from 1.5 to 2.5 meters depth is characterized by a (*p*)-wave velocity  
292 around 185 m/s but shows increases towards 1000 m/s toward the interfaces with the ice core. Our  
293 observed velocity for the very shallow debris layer (0 to 1 m depth ) differs significantly from  
294 previous refraction studies done on DCG, where velocities around 500 m/s have been observed for  
295 the debris mantle (Bucki et al. 2004; Pavoni et al., 2023), though 300 m/s has been observed as  
296 well (Pasquale et al., 2022). Our study differs from the ones noted here in the receiver spacing,  
297 where the other studies used 3 to 15 m, whereas we used 0.5 and 0.3 m on Sourdough and 1 m at  
298 Malaspina, allowing us to characterize the debris layer velocity as gradational and highly variable.  
299 The observed 185 m/s direct wave velocity at near offsets represents the complicated path the  
300 direct arrival has to take to the geophones. The cobbles that make up the debris individually have  
301 a *p*-wave velocity in the range of granitic rocks (5000-6500 m/s), but the odd coupling between  
302 cobbles and large void space between them complicates the path the direct wave has to take  
303 significantly, but for farther offsets the ray paths are able to travel in more consolidated materials.

304 The depths of the modeled velocities agree with the interfaces indicated by the GPR  
305 profiles (Figure 2). A thin layer beneath the loose debris with velocity values between the loose  
306 debris and pure ice values is interpreted as an ice-cemented debris-layer. Velocities approaching  
307 near pure-ice values are modeled starting at 3.5 m depth for Line 1 and 4.5 m for Line 2. The  
308 modeled ray paths for Line 2 extend deeper than those for Line 1, even though the array length is  
309 shorter. This could be due to discontinuous ice-rich zones and a thicker ice-cemented debris layer,  
310 which would not provide a sharp layer interface for the refracted wave to travel along, as observed  
311 for Line 1. Picking the airwave as the first arrival instead of the direct wave results in a debris layer  
312 thickness of roughly twice the GPR-derived thickness, further confirming that these arrivals are  
313 indeed the arrival from the air wave.

314 We assign layer properties used for the reflection forward modeling and as *a priori* values  
 315 for the inversion of the surface-wave data using observed values from the refraction tomography  
 316 results and studies on other glaciers cited in Table 1. The table is a simple 4-layer model  
 317 interpretation of the overall glacier structure and does not consider internal variations of  
 318 compaction within the debris layer, the likely presence of partially ice-cemented debris near the  
 319 surface, or internal debris in the glacier core.  
 320

	Vp (m/s)	$\rho$ (g/cm <sup>3</sup> )	h (m)	Notes
L <sub>1</sub>	185±15*	1.85±0.1 <sup>†</sup>	1.5-2.5	*Slope of direct-wave first arrivals ; <sup>†</sup> Calculated using debris clast density of 2.65g/cm <sup>3</sup> and estimated layer porosity of 0.3 (Anderson & Anderson, 2018) and the bulk density equation <sup>§</sup>
L <sub>2</sub>	1600±400*	1.6±0.1 <sup>†</sup>	1-2	*from observed data ; <sup>†</sup> Average density of permafrost (Kawasaki et al., 1983)
L <sub>3</sub>	3650±150*	0.95±0.05 <sup>†</sup>	12-30	*clean glacial ice velocity from observed data and previous studies (Kohnen., 1974; Press, 1966); <sup>†</sup> Density of glacial ice (Shumskiy, 1960)
L <sub>4</sub>	4800*	2.65 <sup>†</sup>		* <sup>†</sup> meta-sedimentary bedrock estimations (Press, 1966)

321  
 322 **Table 1.** Sourdough Rock Glacier layer properties for the loose debris (L<sub>1</sub>), interpreted ice-  
 323 cemented debris (L<sub>2</sub>), ice-rich core (L<sub>3</sub>), and bedrock (L<sub>4</sub>) using the observed refraction data and  
 324 values from the literature. A range of observed thicknesses (h) from the refraction data and ground-  
 325 penetrating radar measurements. <sup>§</sup> $\rho_b = (1-f)\rho_s$  where  $\rho_b$  is the bulk density, f is the porosity, and  $\rho_s$   
 326 is the particle density.  
 327



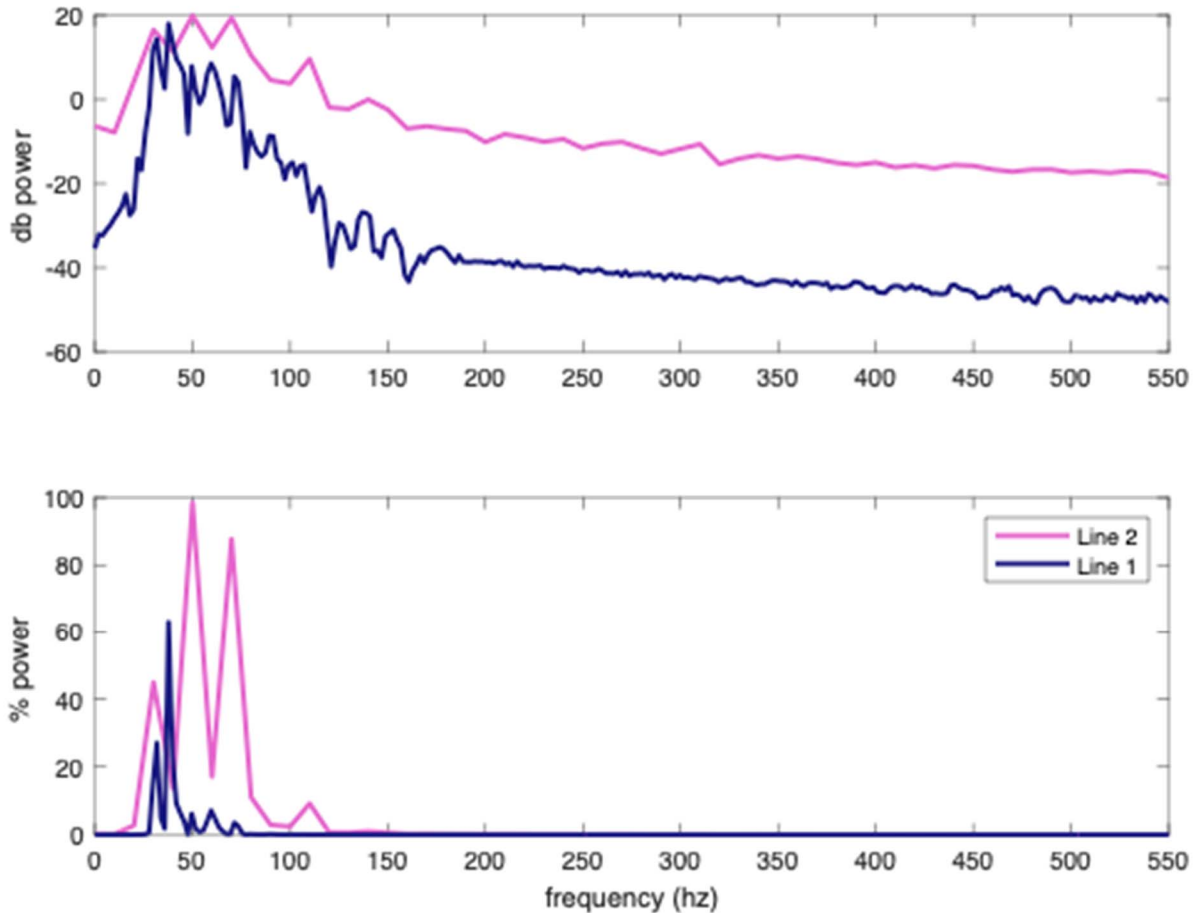
328  
 329 **Figure 5.** Results from the refraction tomography inversions for Sourdough Line 1 (top), Line 2  
 330 (middle), and Malaspina Site 4 (bottom). Modeled ray paths are drawn in red with paths associated  
 331 with multiple rays brighter than paths associated with fewer rays. Receiver locations are shown as  
 332 black dots.  
 333

### 334 3.2 Reflection

#### 335 3.2.1 Reflection Processing

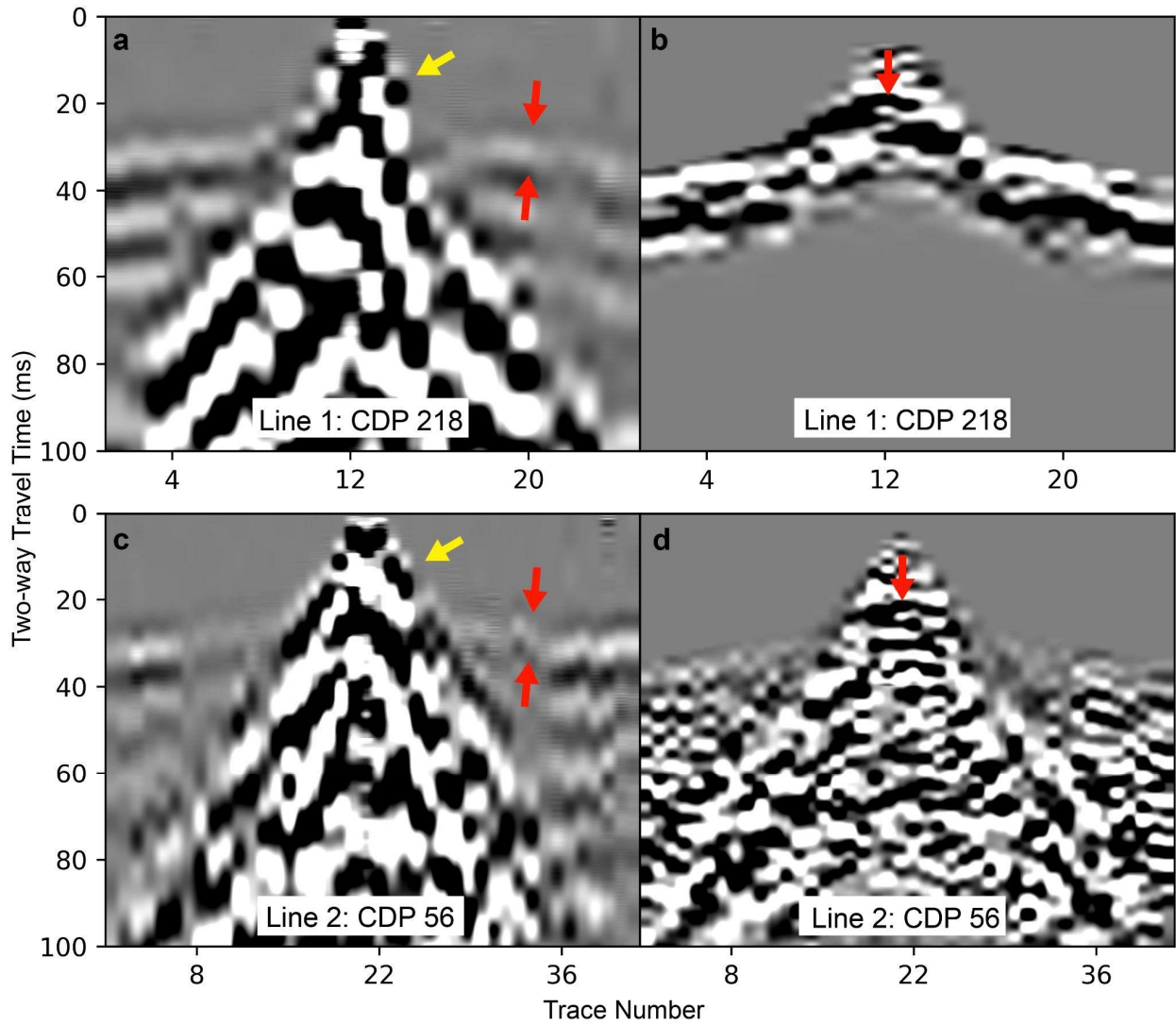
336 For Sourdough reflection processing, individual shot records taken at each station were  
 337 stacked by source location and elevation statics were applied using the replacement velocity of  
 338 185 m/s observed from the first p-wave arrival times to account for the elevation differences  
 339 between the receivers. Spectral analysis of the individual stacked records shows relatively low  
 340  
 341

342 frequencies (Figure 6) for both lines although the frequency response of Line 2 returns higher  
343 frequencies than Line 1 due to the smaller receiver spacing and smaller total array length of the  
344 line. Still, the majority of the recorded frequencies occur below 100 Hz and visual inspection of  
345 the stacked shot records and common depth point (CDP) gathers at high frequencies confirm that  
346 no reflections can be identified when filtering for frequencies above this value for both lines.  
347



348  
349 **Figure 6.** Frequency content of the recorded signal from an example record from Line 1 (0.5 m  
350 receiver spacing, total length = 24 m) and Line 2 (0.3 m receiver spacing, total length = 14.4 m).  
351

352  
353  
354 Using a bandpass filter with corner values at 16-24-140-180 Hz, a reflection hyperbola can  
355 be picked around 21 ms in the high-fold CDP gathers for Line 1 and around 22 ms for Line 2, both  
356 characterized by a normal move-out velocity of  $185 \pm 15$  m/s (figure 7) which becomes asymptotic  
357 to the direct wave. Implementation of a minimum-phase spiking deconvolution filter with a white  
358 noise level of 0.1 was found to increase the resolution of this event and decrease the associated  
359 multiple energy. Additional processing steps included surgical muting to eliminate ground roll and  
360 direct-wave energy. Automatic gain control was also applied.



362

363 **Figure 7.** (a) Raw CDP gather for Line 1 CDP bin #218 with the direct wave denoted by the yellow

364 arrow and the refraction first-arrival wavelet denoted between the two red arrows. (b) after

365 processing and muting the first-arrival energy. (c) Raw CDP gather for Line 2 CDP bin #56 with

366 the same notation as (a). (d) after processing and muting the first-arrival energy. A weak reflection

367 hyperbola indicated by the red arrows can be picked in (b) and (d) with a normal move-out velocity

368 of  $185 \text{ m/s} \pm 15 \text{ m/s}$ . The SEG-YIO python software was used to generate the figure.

369

370

### 370 3.2.2 Synthetic Generation

371

372 To accurately interpret and pick reflection hyperbola in the Sourdough field records, we

373 generate synthetic shot records based on expected velocity structures for both lines. To do this, we

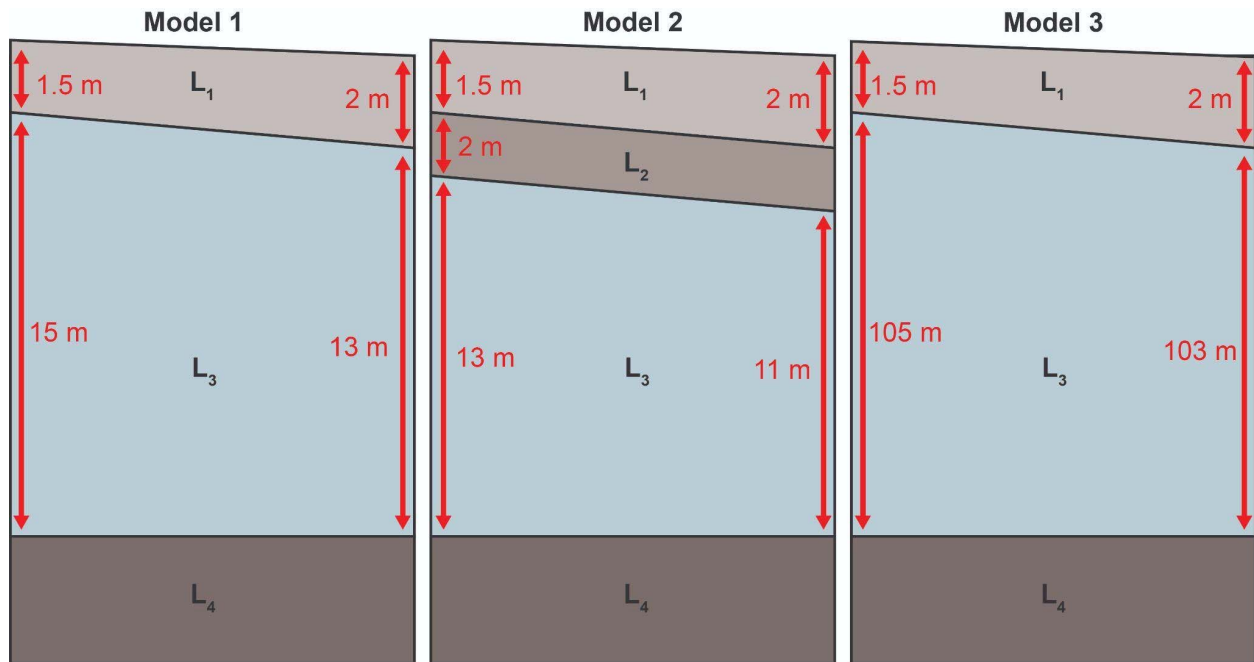
374 use the finite-difference wave propagation modeler SPEC-FEM-2D (Komatitsch, 1997; Komatitsch

375 et al., 1998; Xie et al., 2014) and the layer properties defined in Table 1 to generate the models

376 depicted in Figure 8. The synthetics generated off of these models used the same receiver geometry  
 377 as our field data. Model 1 and Model 2 are simplified representations of the expected structure  
 378 based on the GPR results and observed and expected seismic velocities from Table 1. Model 3  
 379 exaggerates the ice thickness of Model 1 to see if a signal from the glacier bed influences the trace  
 380 data. If a signal from the glacier bed is influencing the synthetic record for Model 1, we should  
 381 observe a change for Model 3, as the bed response would occur at a much later time. The wave  
 382 propagation parameters assume no attenuation factors. The center frequency of the source is  
 383 evaluated at 100 Hz (the frequency of the observed first arrival wavelet in the field records shown  
 384 in Figure 4) and 500 Hz, which allows for easier visual separation of refraction and reflection  
 385 events.

386 It should be noted that while the synthetic models have a shear-wave velocity assigned to  
 387 each layer, they do not accurately represent the complex shear-wave variations within the debris.  
 388 Therefore, the ground-roll Rayleigh waves are not adequately duplicated in the synthetics and an  
 389 analogous surface-wave package cannot be picked. Due to this limitation, we use the synthetic  
 390 shot records as a comparison for potential reflection events only and not for synthetic comparison  
 391 to the field surface-wave data in the MASW inversion process.

392



393

394 **Figure 8.** Representation of the simplified glacier structures used in the synthetic forward  
 395 modeling of Sourdough Line 2. The ( $p$ )-wave and density values for the corresponding layers are  
 396 listed in Table 1. The geometry of the loose debris layer ( $L_1$ ) and ice-cemented debris layers ( $L_2$ )  
 397 are from the GPR and refraction tomography observations. The length along the model  
 398 corresponds to the array length of Line 2.

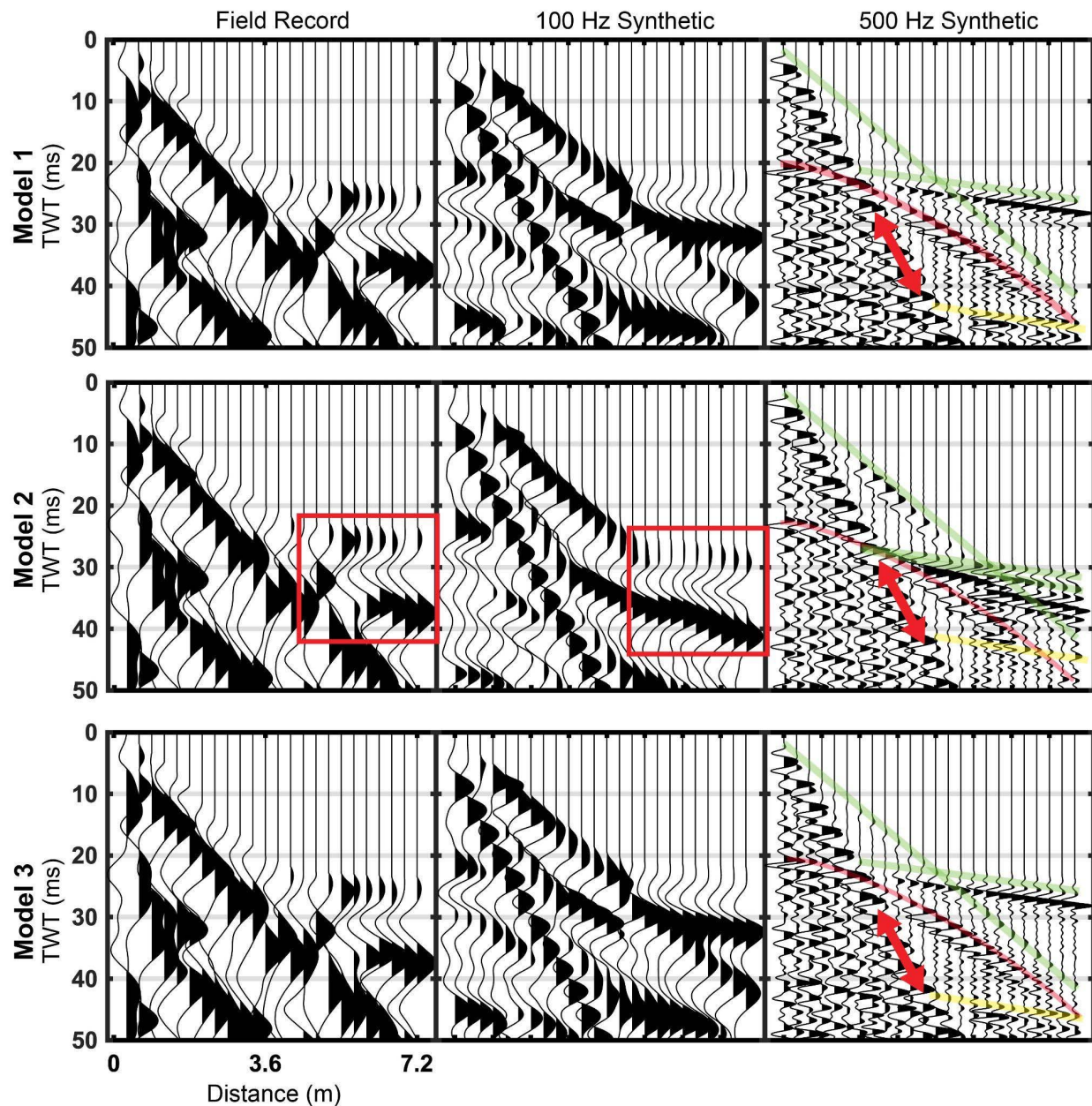
399

400

401 No reflection hyperbolae were visually detectable at later times associated with deeper  
402 interfaces, such as an ice-cemented debris layer or the glacier bed. Figure 9 compares the results  
403 from the synthetic shot records to the field data. Our recorded frequencies show that no discernible  
404 reflections can be picked in the unstacked field records, which we replicate in the 100 Hz  
405 synthetics. The synthetic models at 100 Hz visually match the observed data fairly well, though  
406 Model 2 produces a better match for the farther-offset events noted by the red boxes, possibly due  
407 to the presence of a thin ice-cemented debris layer. There are differences in the first arrivals  
408 between the synthetics and field data, a result of the non-planarity of the layer interfaces and lateral  
409 changes in dip angle, which we could not capture. However, the simplified synthetic structure  
410 provides a general analog to the field data.

411 The lack of an observed bed reflector in the synthetic models can be explained by the  
412 reflection and transmission coefficients of the debris-ice interface (Sheriff & Geldart, 1982).  
413 Reflection and transmission coefficients are strongly affected by the difference in acoustic  
414 impedance (a product of layer density and seismic velocity) of each geologic layer. Table 2 lists  
415 the reflection coefficients for Models 1 and 2 at normal-incidence of a pure-elastic medium using  
416 the layer properties from Table 1. In both models, the debris layer has a very strong reflection  
417 coefficient (Model 1  $R_{\text{mean}} = 0.81$ ; Model 2  $R_{\text{mean}} = 0.749$ ), which prevents source energy from  
418 transmitting to deeper layers as well as the transmitted energy from returning to the surface, which  
419 is below 5% for both models. These calculations do not include attenuation effects from scattering,  
420 geometrical spreading or non-normal incidence, which would decrease the amount of returned  
421 energy even further. This could explain why a deeper reflector, like the one marked by the yellow  
422 arrows in the radar profile (Figure 2) or a glacier-bed reflection does not appear in the individual  
423 seismic shot records or CDP gathers.

424



425  
 426 **Figure 9.** Line 2 Field record (ffid 3255) and synthetic record comparison of model 1 (top), model  
 427 2 (middle), and model 3 (bottom) parameters. The direct wave and refraction events are highlighted  
 428 in green, the bottom of the debris layer reflection hyperbola in red, and refraction multiple in  
 429 yellow. The red double-sided arrow marks the strong surface wave event in the debris layer that  
 430 does not match the field data. The better visual match between the Model 2 far-offset events and  
 431 the field data is outlined by the red boxes.  
 432

**Model 1 & Model 3 Layer Parameters**

Layer Properties	Interface	$R_{\text{mean}} ; T_{\text{mean}}$	Coefficient Range	% Returned to Surface
$L_1 = V_{p1}(185 \pm 15); \rho_1(1.85 \pm 0.1)$	$L_1 / L_2$	0.81 ; 0.19	$\pm 0.03$	81 $\pm$ 3%
$L_2 = V_{p2}(3650 \pm 150); \rho_2(0.95 \pm 0.05)$	$L_2 / L_3$	0.552 ; 0.448	$\pm 0.033$	2.2 $\pm$ 0.77%
$L_3 = V_{p3}(4800); \rho_3(2.65)$				

**Model 2 Layer Parameters**

Layer Properties	Interface	$R_{\text{mean}} ; T_{\text{mean}}$	Coefficient Range	% Returned to Surface
$L_1 = V_{p1}(185 \pm 15); \rho_1(1.85 \pm 0.1)$	$L_1 / L_2$	0.749 ; 0.251	$\pm 0.07$	74.9 $\pm$ 7%
$L_2 = V_{p2}(1600 \pm 400); \rho_2(1.6 \pm 0.1)$	$L_2 / L_3$	0.162 ; 0.838	$\pm 0.148$	1.62 $\pm$ 1.58%
$L_3 = V_{p3}(3650 \pm 150); \rho_3(0.95 \pm 0.05)$	$L_3 / L_4$	0.552 ; 0.448	$\pm 0.033$	3.6 $\pm$ 2.4%
$L_4 = V_{p4}(4800); \rho_4(2.65)$				

433

434

435

436

437

438

439

440

441

442

443

444

445

446

447

448

449

450

451

452

453

454

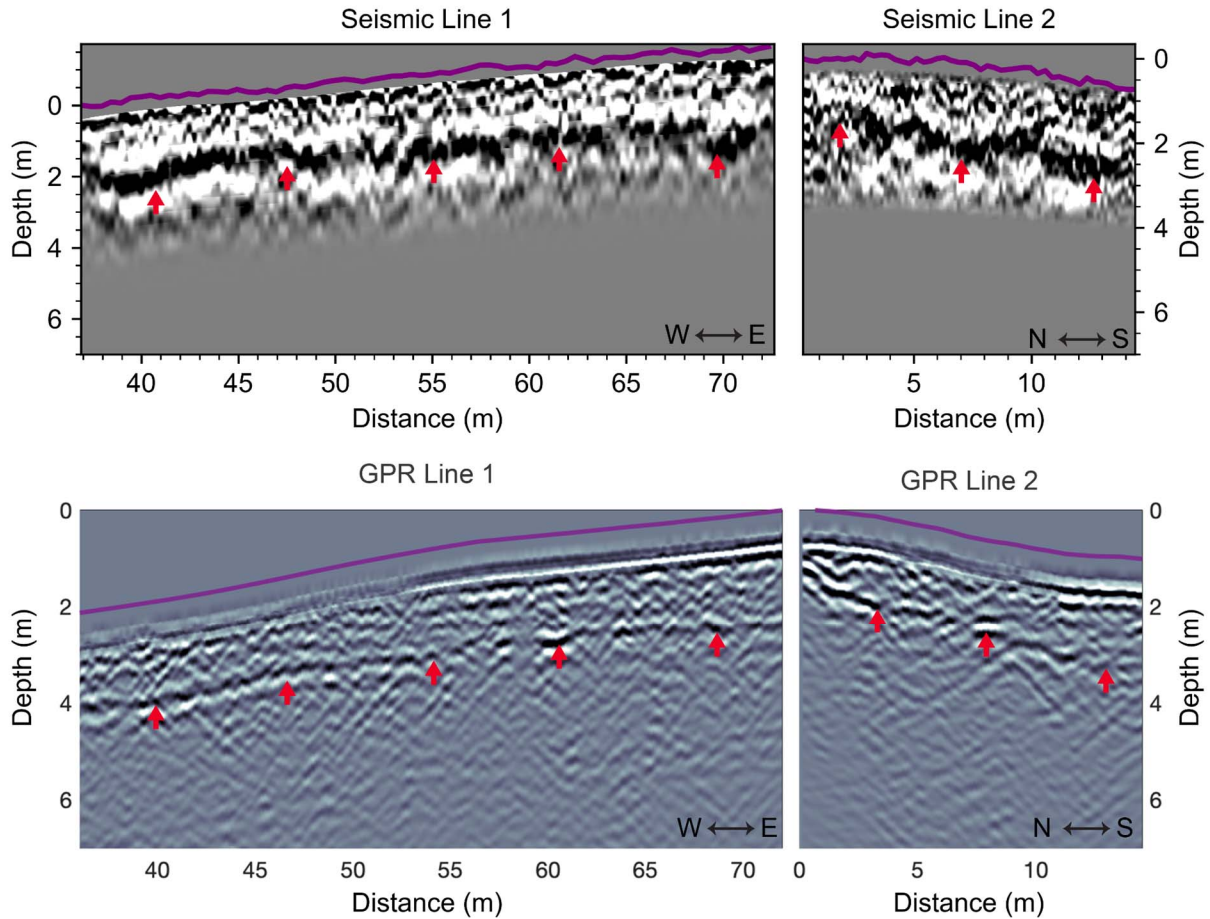
455

456

**Table 2.** Reflection ( $R_{\text{mean}}$ ) and transmission ( $T_{\text{mean}}$ ) coefficients at normal-incidence to the source for the pure-elastic simplified velocity structures modeled in the synthetic shot records (Figure 8) using the Zoeppritz equations (Sheriff & Geldart, 1982). ( $p$ )-wave velocities are in m/s and densities in  $\text{g}/\text{cm}^3$ . The amount of source energy returned to the surface is very high for the bottom of the debris layer and negligible before attenuation effects from deeper layers.

### 3.2.3 Reflection Results & Interpretation

Figure 10 shows the stacked CDP depth sections for the Sourdough reflection surveys. The sections were migrated to depth sections using a velocity of 185 m/s picked from the reflection hyperbolas in the CDPs discussed earlier. The first half of Line 1, for which the source was the 16-lb sledgehammer, yields no reliable reflector and is not imaged in the final results. The lack of a reflector for this portion of the line is probably a result of the signal-to-noise ratio, with much more source-generated noise associated with shots taken with the sledgehammer versus the rock hammer. The last half of Line 1 from meters 37 to 72, where the rock hammer was used as a source, yielded better results. The imaged reflector is interpreted as the bottom of the loose debris layer and agrees with the picked reflector from the coincident GPR data. The closer receiver spacing for Line 2, yields a stronger reflector from the bottom of the loose debris layer and lateral variability of the interface depth is more apparent. Comparing the seismic reflection results to the GPR results (Figure 9), it is apparent that the GPR yields more coherent data, as there is a higher signal to noise ratio than the seismic data. It is encouraging that the picked seismic reflection for the bottom of the loose debris closely matches the behavior of the interpreted reflection from the GPR data.



457  
 458 **Figure 10.** (Top) Seismic Line 1 and Seismic Line 2 processed and stacked CDP sections from  
 459 the Sourdough glacier reflection surveys converted to depth. The reflector denoted by the red  
 460 arrows is interpreted to be the bottom of the loose debris. The purple line indicates the approximate  
 461 topography of the debris surface from GPS data collected at each receiver station and corrected  
 462 for geophone height. Depth = 0 is relative to the surface at the first receiver station in each line.  
 463 (Bottom) The GPR results are corrected for topography and displayed for comparison, with the  
 464 red arrows denoting the bottom of the loose debris. Differences in the topography line are a result  
 465 of using a Topcon SGR-1 DGPS for the PulseEKKO GPR system and a RTK GNSS receiver for  
 466 the seismic geophone locations, which is described in section 2.2.

### 467 3.3 MASW

#### 468 3.3.1 MASW Processing

469

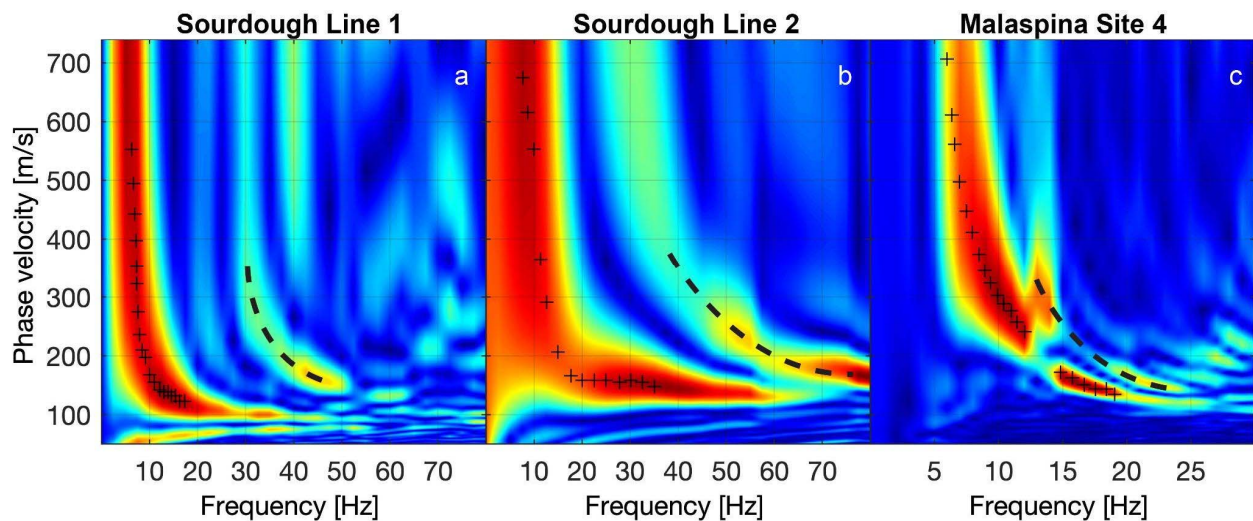
470 Preliminary MASW processing included stacking multiple individual shot records by  
 471 source location and applying a surgical mute to isolate the surface waves. The complex velocity  
 472 structure of the debris layer on Sourdough necessitates custom muting for each stacked shot record  
 473 to accurately isolate the surface waves, while general mutes based on offset could be used for  
 474 Malaspina Site 4. A bandpass filter fitting the frequency spectrum of each site was also applied.

475 The corner frequencies used for the Sourdough lines are 2-4-50-80 Hz. The Malaspina site used a  
476 bandpass filter with frequencies of 2-4-100-120 Hz.

477 A minimum offset of 5.5 m was used when selecting traces for the analysis on Sourdough  
478 to account for near-field effects of non-planar wave propagation. After visual analysis of  
479 dispersion-image coherence, it was determined that a maximum offset of 18 m could be used for  
480 trace selection. Incorporating traces at larger offsets greatly reduced the quality of the dispersion  
481 image. For the Malaspina site, a minimum offset of 6 m was used, while the full line length to 53-  
482 m offset was used as the attenuation effects were much less than for the Sourdough data.

483 To extract the experimental dispersion curve from the shot records, the software  
484 MASWaves (Olafsdottir et al., 2018) was used. MASWaves applies a Fourier transform to the  
485 trace data, normalizing for each phase velocity and wavelength set, and summing the set  
486 amplitudes to create a dispersion image (Figure 10). The experimental dispersion curve was then  
487 manually picked from the peak values of the dispersion image. We then inverted the picked  
488 fundamental mode of the dispersion curve to yield a 1-dimensional shear-wave ( $V_s$ ) velocity  
489 profile in the MASWaves software. A limitation of MASWaves is that higher modes of the  
490 dispersion image are not able to be accounted for in the inversion process. A multi-modal inversion  
491 process could lead to more accurate results and a larger depth of investigation.

492



493

494

495 **Figure 11.** Examples of normalized amplitude dispersion spectrum images from Sourdough Line  
496 1 (a), Line 2 (b), and Malaspina forelands Site 4 (c). The picked fundamental mode of the  
497 dispersion curve is marked with black crosses and identified strong first higher modes as dashed  
498 black lines.

499

### 500 3.3.2 MASW Results & Interpretation

501

502 Examples from Sourdough indicate that with close receiver spacing and source offset  
503 limited to a maximum of 18 m, a reliable and clean dispersion curve can be extracted from the

504 surface-wave package. The Sourdough curves display strong frequency amplitude below 10 Hz  
505 (Figure 11 a,b) even with 40-Hz geophones. The curve for Line 2 is smoother compared to Line 1,  
506 indicating that closer receiver spacing leads to a more defined curve, although this could also be  
507 due to differences in velocity structure, as the debris cover is a laterally complex medium. The  
508 fundamental mode of the Malaspina site shot record displays a jump to the first higher mode around  
509 12 Hz and a sharp step back down to the fundamental mode around 16 Hz (Figure 10c). This break  
510 to a higher mode indicates that the surface-wave energy is influenced by a sharp velocity contrast  
511 at depth. The extracted Sourdough dispersion curves do not display a break to a higher mode at  
512 low frequencies, likely indicating that the surface waves are not traveling through an interface with  
513 high velocity contrast as we expect for the debris layer and ice-rich glacier core.

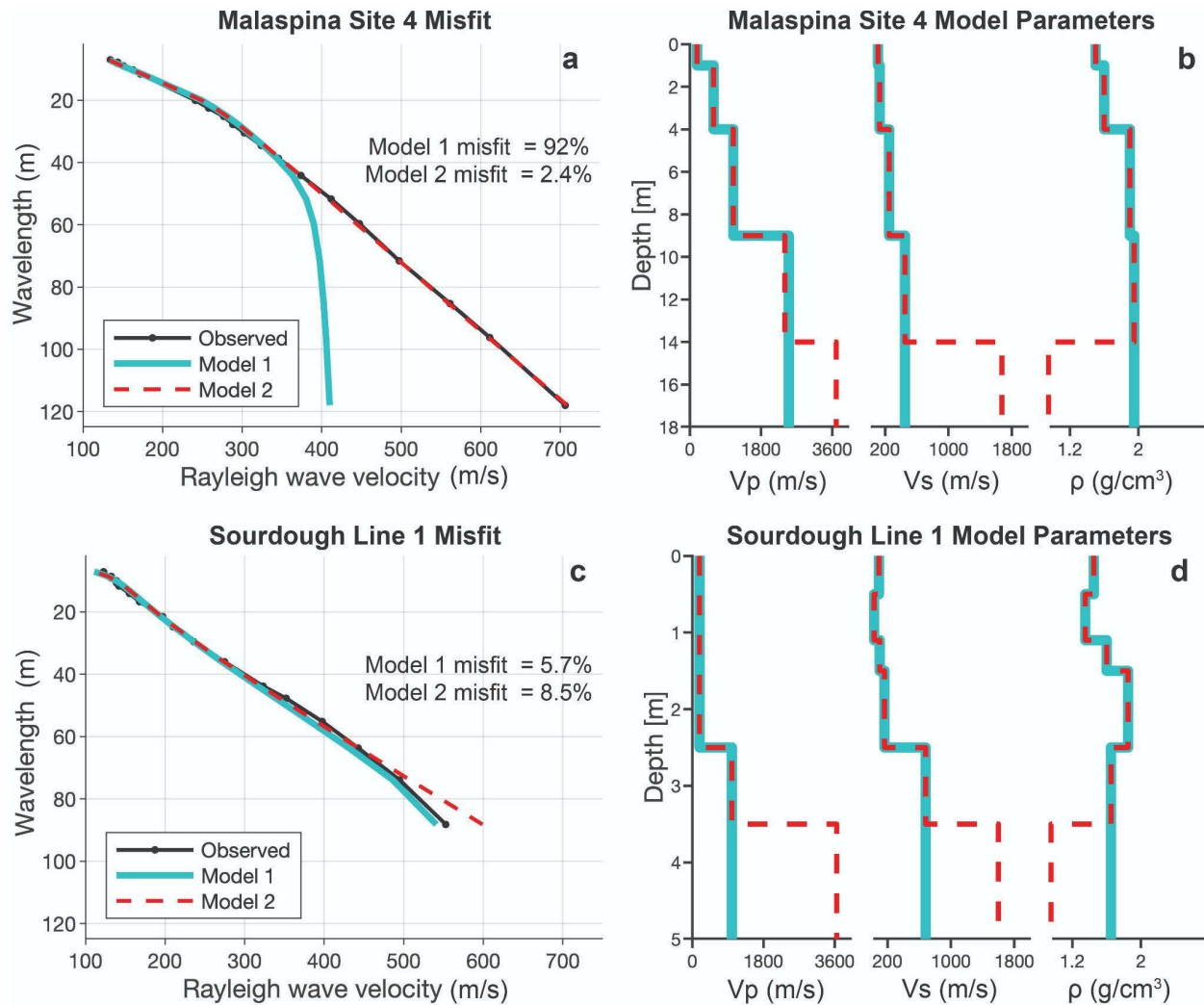
514 Figure 12(a,b) shows the results from the fundamental mode inversion of the modeled  
515 velocity structure at Malaspina Site 4. The best fit for layer model 1 which uses  $V_p$ ,  $V_s$ , and  $\rho$   
516 parameters analogous to a till debris layer which compacts with depth over a till halfspace at 14-  
517 m depth has a normalized root-mean-squared error (NRMSE) of 92%. The error for model 2,  
518 which uses the same thickness,  $V_p$ ,  $V_s$ , and  $\rho$  parameters for the debris layer as model 1, but  
519 incorporates parameters for an ice-rich half-space at 14 m depth is 2.4 %. From this we conclude  
520 that the extracted dispersion curve for this Malaspina site depends heavily on surface waves from  
521 an ice-rich layer depth.

522 Figure 12(c,d) displays the inversion for an example record from Sourdough Line 1. The  
523 best-fitting Model 1 parameters are analogous to an ice-cemented debris half-space starting at 2.5  
524 m depth and Model 2 adds parameters analogous to an ice-rich half-space at 3.5 m depth. The  
525 NRMSE for Model 1 is 5.7 % and the NRMSE for Model 2 is 8.5 %. From these errors, it can be  
526 concluded that any surface waves being generated in the ice-rich core are not affecting our  
527 observed fundamental mode. As we noted earlier, a full-waveform analysis and multi-modal  
528 inversion scheme could provide a higher depth of investigation.

529 Sourdough Model 1 indicates that the surface waves are very sensitive to the complex  
530 velocity structure within the debris and ice-cemented debris layers. The 5-layer model shows that  
531 the debris layer can be characterized by an ( $s$ )-wave range of 30-160 m/s. The model supports an  
532 increase to an ( $s$ )-wave velocity of 680 m/s at 2.5 m depth, which is below the typical permafrost  
533 ( $s$ )-wave range of 1000-1650 m/s and massive ice range of 1550-2050 m/s (Killingbeck et al.,  
534 2018; Press, 1966; Tsoflias et al., 2008; Yang et al., 2011). This could indicate that at 2.5-m depth  
535 there is some ice-cementation but voids or melt could also be present.

536 The results for the MASW inversions are consistent with a sharp transition to high-purity  
537 ice at approximately 14 m depth at the site in the Malaspina forelands. It supports the previously  
538 discussed observations that the debris layer on Sourdough is laterally elastically complex, but  
539 ultimately gets more consolidated with depth.

540



541  
 542 **Figure 12.** Results of the fundamental-mode inversion process for Vs models analogous to an  
 543 ice-rich halfspace (red dashed line) and an ice-cemented debris halfspace (blue). The observed  
 544 dispersion curve is plotted in black in (a) and (c) against the models. The forward model input  
 545 parameters Vp, Vs, and  $\rho$  are plotted in (b) and (d).

546 **4 Discussion & Conclusions**

547  
 548 The primary goal of this study was to image the shallow debris-ice interface of DCG using  
 549 active seismic methods and to yield more useful information from the seismic record than just the  
 550 refraction first arrivals. Previous exploration studies using active seismic methods have so far been  
 551 limited to refraction analysis, but we demonstrate that ultra-dense arrays generate more high-  
 552 quality information for extraction from the seismic shot records, and the methods can be useful for  
 553 characterizing the elastic parameters of the very shallow subsurface of these glaciers.

554 While GPR offers advantages over active seismic methods in terms of field logistics and  
 555 quality of the results for imaging reflections, the results from the surface-wave survey are  
 556 intriguing from the perspective of characterizing the elastic properties of the debris layer. The

557 depth of investigation for surface-wave methods is heavily dependent on energy of the source and  
558 the physical properties of the debris. Depths of investigation in the range of tens of meters can be  
559 achieved on sites with consolidated debris cover similar to the Malaspina forelands site, while the  
560 investigation is limited to only the upper few meters on loose debris surfaces such as the Sourdough  
561 site. Future studies implementing higher modes during the MASW inversion process could  
562 provide elastic parameters of the deeper subsurface. Logical next steps could provide joint  
563 inversions between 2D MASW results and p-wave refraction tomography to get a  $V_p/V_s$  ratio  
564 image could further constrain zones of consolidation or void space within this layer. When  
565 combined with electrical resistivity surveys, this could help the interpretation of void space, zones  
566 of melt in the debris layer, snow compaction within the debris and debris entrainment within the  
567 ice.

568 While we are able to image a reflection from the survey on Sourdough, it is apparent that  
569 GPR methods can provide more reliable and precise reflection measurements due to the  
570 frequencies involved and the higher signal to noise ratio of the acquired data, allowing it to have  
571 the ability to image the deeper reflections in the subsurface on these glacial features. Shortfalls of  
572 the GPR method though are the uncertainty in the dielectric permittivity of the debris and an  
573 assumed velocity for the whole section. In this regard seismic methods can provide insight, as the  
574 velocities are observed from the data, which reduces uncertainty in the interpretation. We were  
575 able to image a reflection from the bottom of the loose debris layer, which was the primary goal  
576 of the reflection work on Sourdough. Secondary goals of imaging deeper reflections were not  
577 successful, which we explain by the fundamental acoustic properties of the velocity structure and  
578 synthetic record comparison. We observe that high-frequency filtering, typically above 400 Hz for  
579 ultra-shallow reflection processing (Steeple & Miller, 1998), is not possible with reflection data  
580 collected on debris-covered glaciers and rock glaciers due to the highly attenuating nature of the  
581 debris layer. Most of the recorded frequency values occur in the 20-60 Hz range and no coherent  
582 signals appear in the individual shot records or CDP gathers when looking at high frequency-  
583 filtering windows.

584 Future surveys investigating the shallow structure of debris-covered glaciers could be  
585 designed using distributed acoustic sensing (DAS). As we have shown, results can be achieved  
586 with very small receiver spacings, which makes DAS a logical next step since measurements can  
587 be recorded at any point along the fiber optic cable. DAS uses Rayleigh backscattering from a laser  
588 impulse to record vibrations or changes along a fiber optic cable (Kingsley, 1986) generated by a  
589 source at any point along the cable. While field efficiency for active seismic DAS surveys would  
590 be much greater than setting up a traditional geophone array like this survey uses, further work to  
591 understand the coupling between a DAS cable and the debris surface would need to be examined,  
592 although preliminary work (Spikes et al., 2019) indicates that coupling of fiber optic cables would  
593 be sufficient for such investigations.

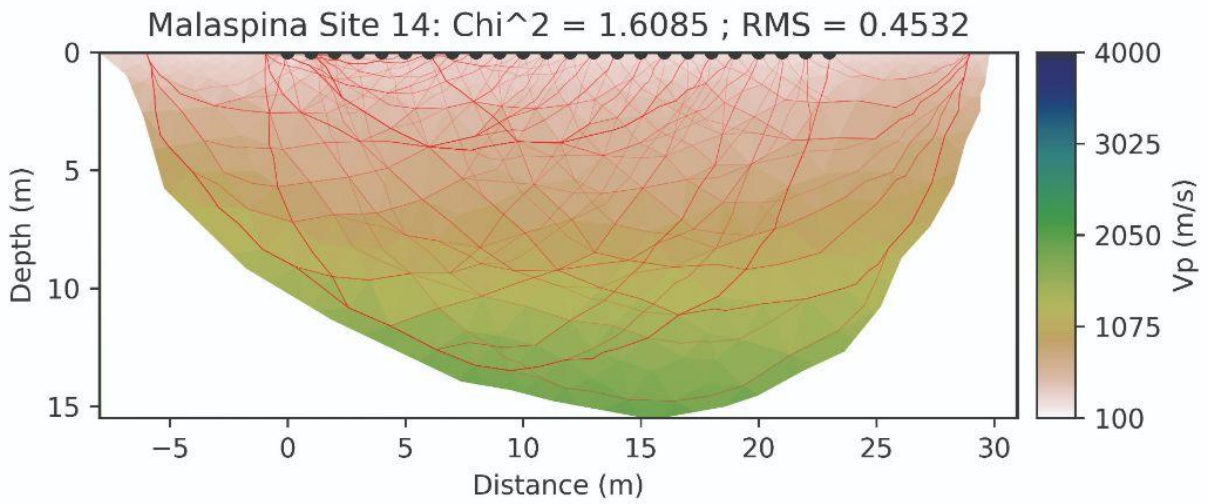
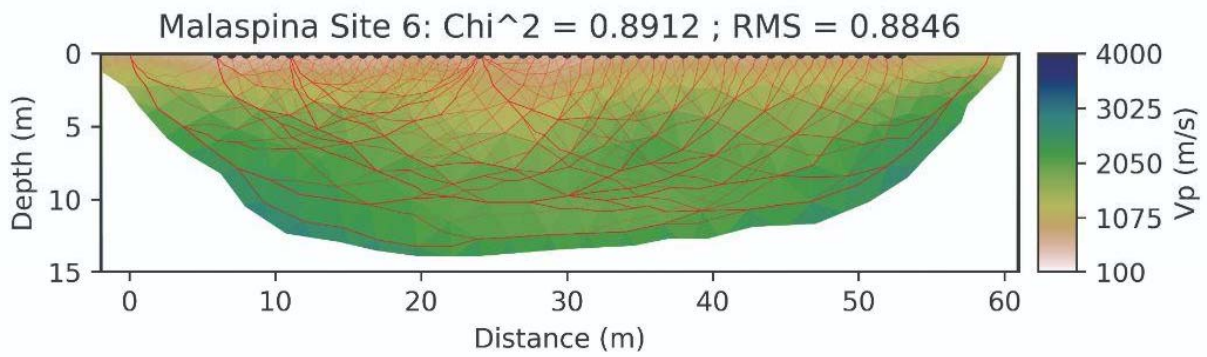
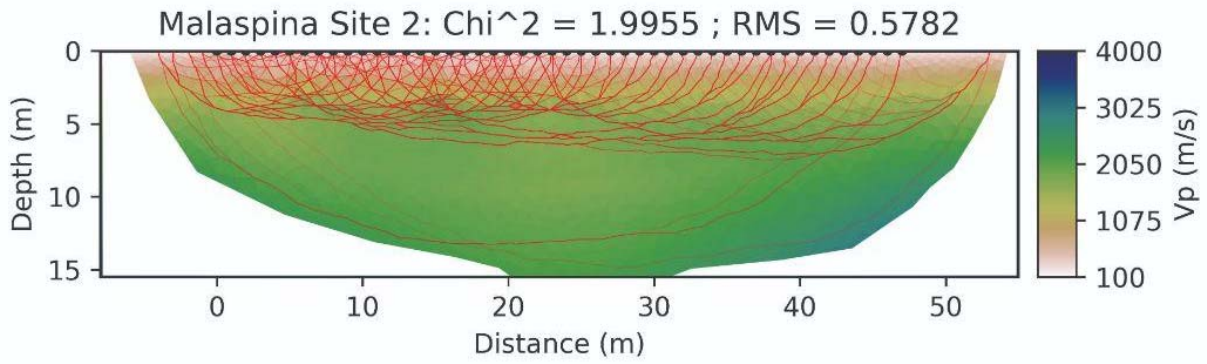
## 594 **Acknowledgements**

595

596 This work was funded by The University of Arizona and National Science Foundation Grant  
597 1929577. We thank Wrangell- St. Elias National Park for the permit to carry out field research in  
598 Malaspina Glacier and Mike Loso of the NPS for his field coordination efforts. We thank our  
599 colleague from the University of Alaska Fairbanks Martin Truffer for including this work in the  
600 scope of the Malaspina surveys. We thank Brandon Tober, Stefano Nerozzi, Michael  
601 Christoffersen, Victor Devaux-Chupin and Natalie Wagner for their assistance in the field data  
602 acquisition. We also thank Brady Flinchum of Clemson University for advice and modification of  
603 his pyGiMLI scripts.

#### 604 **Open Research**

605  
606 The SEG-Y shot record data for the Sourdough glacier acquisition is archived under seismic  
607 network code 2E\_2021 at the IRIS PASSCAL DMC and can be requested using dataset report  
608 number 22-003 (Holt, 2021). SEG-Y data for the Malaspina glacier acquisition is archived under  
609 seismic network code 3J\_2021 at the IRIS PASSCAL DMC and can be requested using dataset  
610 report number 22-007 (Truffer et al, 2021). The GIS data collected for each site, GPR data in segy  
611 format, parameter files for the SPECSEM2D modeling, and example scripts for the refraction  
612 tomography, MASW and reflection image plotting are available at (Kuehn, 2023)  
613 <https://doi.org/10.25422/azu.data.19758499>.

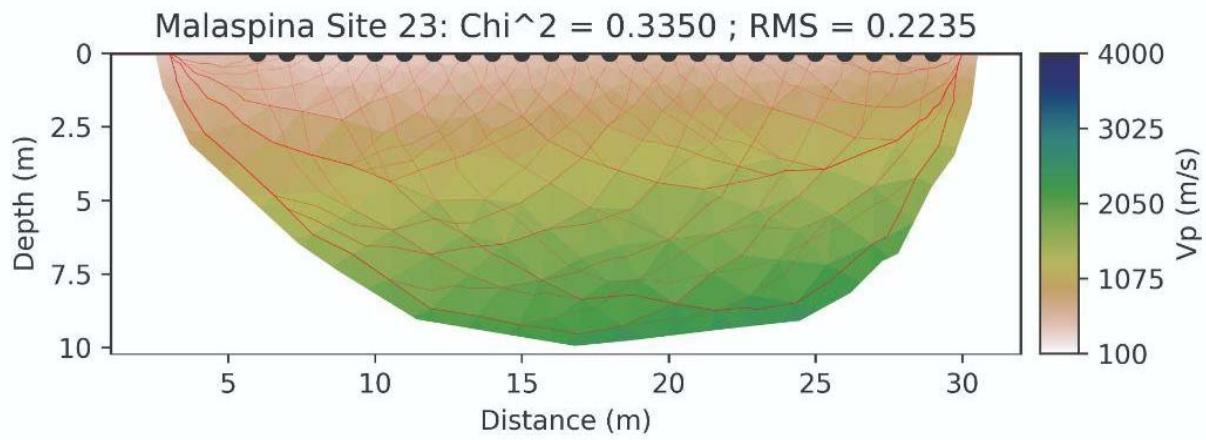
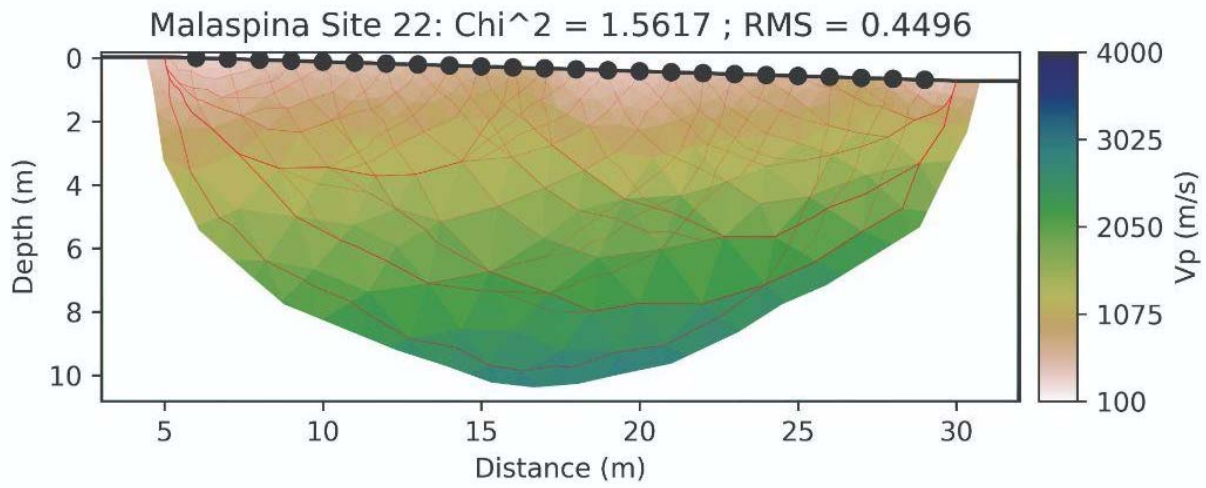


615

616

617

618



619

620

621 **References**

622

623 Abbud-Madrid, Angel, Beaty, D., Boucher, D., Bussey, B., Davis, R., Gertsch, L., Hays, L.,  
624 Kleinhenz, J., Meyer, M., Moats, M., Mueller, R., Paz, A., Suzuki, N., van Susante, P.,  
625 Whetsel, C., & Zbinden, E. (2016, April 22). *Mars Water In-Situ Resource Utilization*  
626 *(ISRU) Planning (M-WIP) Study*.

627 [https://www.researchgate.net/publication/301614744\\_Mars\\_Water\\_In-](https://www.researchgate.net/publication/301614744_Mars_Water_In-Situ_Resource_Utilization_ISRU_Planning_M-WIP_Study)  
628 [Situ\\_Resource\\_Utilization\\_ISRU\\_Planning\\_M-WIP\\_Study](https://www.researchgate.net/publication/301614744_Mars_Water_In-Situ_Resource_Utilization_ISRU_Planning_M-WIP_Study)

629 Allen, C. R., & Smith, G. I. (1953). Seismic and gravity investigations on the Malaspina Glacier,  
630 Alaska. *Transactions, American Geophysical Union*, 34(5), 755.

631 <https://doi.org/10.1029/TR034i005p00755>

632 Baker, G. S., Strasser, J. C., Evenson, E. B., Lawson, D. E., Pyke, K., & Bigl, R. A. (2003).  
633 Near-surface seismic reflection profiling of the Matanuska Glacier, Alaska.

634 *GEOPHYSICS*, 68(1), 147–156. <https://doi.org/10.1190/1.1543202>

635 Bhardwaj, A., Joshi, P. K., Snehmani, Singh, M. K., Sam, L., & Gupta, R. D. (2014). Mapping  
636 debris-covered glaciers and identifying factors affecting the accuracy. *Cold Regions*  
637 *Science and Technology*, 106–107, 161–174.

638 <https://doi.org/10.1016/j.coldregions.2014.07.006>

639 Brabham, P. J., Thomas, J., & McDonald, R. J. (2005). The terrestrial shallow seismic reflection  
640 technique applied to the characterization and assessment of shallow sedimentary  
641 environments. *Quarterly Journal of Engineering Geology and Hydrogeology*, 38(1), 23–  
642 38. <https://doi.org/10.1144/1470-9236/04-033>

643 Bucki, A., Echelmeyer, K., & MacInnes, S. (2004). The thickness and internal structure of  
644 Fireweed rock glacier, Alaska, U.S.A., as determined by geophysical methods. *Journal*  
645 *of Glaciology*, 50(168), 67-75. doi:10.3189/172756504781830196

646 Campbell, M. J., & Ulrichs, J. (1969). Electrical properties of rocks and their significance for

647 lunar radar observations. *Journal of Geophysical Research*, 74(25), 5867–5881.  
648 <https://doi.org/10.1029/JB074i025p05867>

649 Croce, F. A., & Milana, J. P. (2002). Internal structure and behaviour of a rock glacier in the Arid  
650 Andes of Argentina. *Permafrost and Periglacial Processes*, 13(4), 289–299.  
651 <https://doi.org/10.1002/ppp.431>

652 de Pasquale, G., Valois, R., Schaffer, N., and MacDonell, S.: Contrasting geophysical  
653 signatures of a relict and an intact Andean rock glacier. *The Cryosphere*, 16, 1579–  
654 1596, <https://doi.org/10.5194/tc-16-1579-2022>, 2022.

655 Dix, C. H. (1955). Seismic velocities from surface measurements. *GEOPHYSICS*, 20(1), 68–86.  
656 <https://doi.org/10.1190/1.1438126>

657 Flinchum, B. A., Holbrook, W. S., & Carr, B. J. (2022). What Do P-Wave Velocities Tell Us  
658 About the Critical Zone? *Frontiers in Water*, 3.  
659 <https://www.frontiersin.org/article/10.3389/frwa.2021.772185>

660 Florentine, C., Skidmore, M., Speece, M., Link, C., & Shaw, C. A. (2014). Geophysical analysis  
661 of transverse ridges and internal structure at Lone Peak Rock Glacier, Big Sky,  
662 Montana, USA. *Journal of Glaciology*, 60(221), 453–462.  
663 <https://doi.org/10.3189/2014JoG13J160>

664 Foti, S., Hollender, F., Garofalo, F., Albarello, D., Asten, M., Bard, P.-Y., Comina, C., Cornou,  
665 C., Cox, B., Di Giulio, G., Forbriger, T., Hayashi, K., Lunedei, E., Martin, A., Mercerat,  
666 D., Ohrnberger, M., Poggi, V., Renalier, F., Sicilia, D., & Socco, V. (2018). Guidelines for  
667 the good practice of surface wave analysis: A product of the InterPACIFIC project.  
668 *Bulletin of Earthquake Engineering*, 16(6), 2367–2420. [https://doi.org/10.1007/s10518-](https://doi.org/10.1007/s10518-017-0206-7)  
669 [017-0206-7](https://doi.org/10.1007/s10518-017-0206-7)

670 Gustavson, T. C., & Boothroyd, J. C. (1987). A depositional model for outwash, sediment  
671 sources, and hydrologic characteristics, Malaspina Glacier, Alaska: A modern analog of  
672 the southeastern margin of the Laurentide Ice Sheet. *GSA Bulletin*, 99(2), 187–200.

673 [https://doi.org/10.1130/0016-7606\(1987\)99<187:ADMFO>2.0.CO;2](https://doi.org/10.1130/0016-7606(1987)99<187:ADMFO>2.0.CO;2)

674 Head, J. W., Marchant, D. R., Dickson, J. L., Kress, A. M., & Baker, D. M. (2010). Northern mid-  
675 latitude glaciation in the Late Amazonian period of Mars: Criteria for the recognition of  
676 debris-covered glacier and valley glacier landsystem deposits. *Earth and Planetary  
677 Science Letters*, 294(3), 306–320. <https://doi.org/10.1016/j.epsl.2009.06.041>

678 Heincke, B., Günther, T., Dalsegg, E., Rønning, J. S., Ganerød, G. V., & Elvebakk, H. (2010).  
679 Combined three-dimensional electric and seismic tomography study on the Åknes  
680 rockslide in western Norway. *Journal of Applied Geophysics*, 70(4), 292–306.  
681 <https://doi.org/10.1016/j.jappgeo.2009.12.004>

682 Holt, J. W., Safaeinili, A., Plaut, J. J., Head, J. W., Phillips, R. J., Seu, R., Kempf, S. D.,  
683 Choudhary, P., Young, D. A., Putzig, N. E., Biccari, D., & Gim, Y. (2008). Radar  
684 Sounding Evidence for Buried Glaciers in the Southern Mid-Latitudes of Mars. *Science*,  
685 322(5905), 1235–1238. <https://doi.org/10.1126/science.1164246>

686 Holt, J.W. (2021). Reflection and Refraction Active Seismic Acquisition on Sourdough Rock  
687 Glacier, McCarthy, Alaska [Data set]. International Federation of Digital Seismograph  
688 Networks. [https://doi.org/10.7914/SN/2E\\_2021](https://doi.org/10.7914/SN/2E_2021)

689 Karlı, H., & Bayrak, Y. (2004). Using the Wiener–Levinson algorithm to suppress ground-roll.  
690 *Journal of Applied Geophysics*, 55(3–4), 187–197.  
691 <https://doi.org/10.1016/j.jappgeo.2003.11.003>

692 Killingbeck, S. F., Livermore, P. W., Booth, A. D., & West, L. J. (2018). Multimodal layered  
693 transdimensional inversion of seismic dispersion curves with depth  
694 constraints. *Geochemistry, Geophysics, Geosystems*, 19, 4957–  
695 4971. <https://doi.org/10.1029/2018GC008000>

696 Kingsley, S. A. (1986). Distributed Fiber-Optic Sensors: An Overview. *Fiber Optic and Laser  
697 Sensors III*, 0566, 28–36. <https://doi.org/10.1117/12.949760>

698 Komatitsch, D. (1997). *Méthodes spectrales et éléments spectraux pour l'équation de*

699 *l'élastodynamique 2D et 3D en milieu hétérogène*. Institut de Physique du Globe de  
700 Paris.

701 Komatitsch, D., Tromp, Jeroen, & Vilotte, Jean-Pierre. (1998). The spectral element method for  
702 elastic wave equations: Application to 2D and 3D. *Bulletin of the Seismological Society*  
703 *of America*, 88, 368–392.

704 Kuehn, T. (2023). Active Seismic Refraction, Reflection and Surface-Wave Exploration in  
705 Debris-Covered Glacial Environments, Sourdough and Malaspina Glaciers, Alaska  
706 [Dataset]. University of Arizona Research Data Repository.  
707 <https://doi.org/10.25422/azu.data.19758499.v1>

708 Langston, G., Bentley, L. R., Hayashi, M., McClymont, A., & Pidlisecky, A. (2011). Internal  
709 structure and hydrological functions of an alpine proglacial moraine. *Hydrological*  
710 *Processes*, 25(19), 2967–2982. <https://doi.org/10.1002/hyp.8144>

711 Levy, J. S., Fassett, C. I., Head, J. W., Schwartz, C., & Watters, J. L. (2014). Sequestered  
712 glacial ice contribution to the global Martian water budget: Geometric constraints on the  
713 volume of remnant, midlatitude debris-covered glaciers. *Journal of Geophysical*  
714 *Research: Planets*, 119(10), 2188–2196. <https://doi.org/10.1002/2014JE004685>

715 Maurer, H., & Hauck, C. (2007). Geophysical imaging of alpine rock glaciers. *Journal of*  
716 *Glaciology*, 53(180), 110–120. <https://doi.org/10.3189/172756507781833893>

717 Meng, T., Petersen, E., & Holt, J. (2022). Rock glacier composition and structure from radio  
718 wave speed analysis with dipping reflector correction. *Journal of Glaciology*, 1-19.  
719 [doi:10.1017/jog.2022.90](https://doi.org/10.1017/jog.2022.90)

720 Merz, K., Maurer, H., Rabenstein, L., Buchli, T., Springman, S. M., & Zweifel, M. (2016).  
721 Multidisciplinary geophysical investigations over an alpine rock glacier. *GEOPHYSICS*,  
722 81(1), WA147–WA157. <https://doi.org/10.1190/geo2015-0157.1>

723 Monnier, S., & Kinnard, C. (2013). Internal structure and composition of a rock glacier in the  
724 Andes (upper Choapa valley, Chile) using borehole information and ground-penetrating

725 radar. *Annals of Glaciology*, 54(64), 61–72. <https://doi.org/10.3189/2013AoG64A107>

726 Musgrave, A. W. (Ed.). (1967). *Seismic Refraction Prospecting*. Society of Exploration  
727 Geophysicists. <https://doi.org/10.1190/1.9781560802679>

728 Musil, M., Maurer, H., Green, A. G., Horstmeyer, H., Nitsche, F. O., Mühl, D. V., & Springman,  
729 S. (2002). Shallow seismic surveying of an Alpine rock glacier. *GEOPHYSICS*, 67(6),  
730 1701–1710. <https://doi.org/10.1190/1.1527071>

731 Nicholson, L., & Benn, D. I. (2006). Calculating ice melt beneath a debris layer using  
732 meteorological data. *Journal of Glaciology*, 52(178), 463–470.  
733 <https://doi.org/10.3189/172756506781828584>

734 Olafsdottir, E. A., Erlingsson, S., & Bessason, B. (2018). Tool for analysis of multichannel  
735 analysis of surface waves (MASW) field data and evaluation of shear wave velocity  
736 profiles of soils. *Canadian Geotechnical Journal*, 55(2), 217–233.  
737 <https://doi.org/10.1139/cgj-2016-0302>

738 Östrem, G. (1959). Ice Melting under a Thin Layer of Moraine, and the Existence of Ice Cores in  
739 Moraine Ridges. *Geografiska Annaler*, 41(4), 228–230.

740 Park, C. B., Miller, R. D., & Miura, H. (2002). *Optimum Field Parameters of an MASW Survey*. 6.

741 Park, C. B., Miller, R. D., & Xia, J. (1999). Multichannel analysis of surface waves.  
742 *GEOPHYSICS*, 64(3), 800–808. <https://doi.org/10.1190/1.1444590>

743 Park, C. B., Miller, R. D., Xia, J., & Ivanov, J. (2007). Multichannel analysis of surface waves  
744 (MASW)—Active and passive methods. *The Leading Edge*, 26(1), 60–64.  
745 <https://doi.org/10.1190/1.2431832>Paul, F., Huggel, C., & Käab, A. (2004). Combining  
746 satellite multispectral image data and a digital elevation model for mapping debris-  
747 covered glaciers. *Remote Sensing of Environment*, 89(4), 510–518.  
748 <https://doi.org/10.1016/j.rse.2003.11.007>

749 Pavoni, M., Boaga, J., Wagner, F.M., Bast, A., Phillips, M. (2023). Characterization of rock  
750 glaciers environments combining structurally-coupled and petrophysically-coupled joint

751           inversions of electrical resistivity and seismic refraction datasets. *Journal of Applied*  
752           *Geophysics*, 215. <https://doi.org/10.1016/j.jappgeo.2023.105097>.

753   Petersen, E. I., Holt, J. W., Stuurman, C. M., Levy, J. S., Nerozzi, S., Paine, J. G., Larsen, C. F.,  
754           & Fahnestock, M. (2016). Sourdough Rock Glacier, Alaska: An Analog to Martian  
755           Debris-Covered Glaciers. *47th Lunar and Planetary Science Conference*, 2.

756   Petersen, E. I., Levy, J. S., Holt, J. W., & Stuurman, C. M. (2020). New insights into ice  
757           accumulation at Galena Creek Rock Glacier from radar imaging of its internal structure.  
758           *Journal of Glaciology*, 66(255), 1–10. <https://doi.org/10.1017/jog.2019.67>

759   Potter, N., Jr. (1972). Ice-Cored Rock Glacier, Galena Creek, Northern Absaroka Mountains,  
760           Wyoming. *GSA Bulletin*, 83(10), 3025–3058. [https://doi.org/10.1130/0016-](https://doi.org/10.1130/0016-7606(1972)83[3025:IRGGCN]2.0.CO;2)  
761           7606(1972)83[3025:IRGGCN]2.0.CO;2

762   Press, F. (1966). SECTION 9: SEISMIC VELOCITIES. In *Geological Society of America*  
763           *Memoirs* (Vol. 97, pp. 195–218). Geological Society of America.  
764           <https://doi.org/10.1130/MEM97-p195>

765   Richart, F.E., Hall, J.R., & Woods, R.D. (1970). *Vibrations of soils and foundations*. Prentice-  
766           Hall, Inc.

767   Ronczka, M., Hellman, K., Günther, T., Wisén, R., & Dahlin, T. (2017). Electric resistivity and  
768           seismic refraction tomography: A challenging joint underwater survey at Äspö Hard Rock  
769           Laboratory. *Solid Earth*, 8(3), 671–682. <https://doi.org/10.5194/se-8-671-2017>

770   Rowan, A. V., Egholm, D. L., Quincey, D. J., & Glasser, N. F. (2015). Modelling the feedbacks  
771           between mass balance, ice flow and debris transport to predict the response to climate  
772           change of debris-covered glaciers in the Himalaya. *Earth and Planetary Science Letters*,  
773           430, 427–438. <https://doi.org/10.1016/j.epsl.2015.09.004>

774   Rücker, C., Günther, T., & Wagner, F. M. (2017). pyGIMLi: An open-source library for modelling  
775           and inversion in geophysics. *Computers & Geosciences*, 109, 106–123.  
776           <https://doi.org/10.1016/j.cageo.2017.07.011>

777 Russell, I. C. (1893). Malaspina Glacier. *The Journal of Geology*, 1(3), 219–245.

778 Sauber, J., Molnia, B., Carabajal, C., Luthcke, S., & Muskett, R. (2005). Ice elevations and  
779 surface change on the Malaspina Glacier, Alaska. *Geophysical Research Letters*,  
780 32(23). <https://doi.org/10.1029/2005GL023943>

781 Scherler, D., Bookhagen, B., & Strecker, M. R. (2011). Spatially variable response of Himalayan  
782 glaciers to climate change affected by debris cover. *Nature Geoscience*, 4(3), Article 3.  
783 <https://doi.org/10.1038/ngeo1068>

784 Sheriff, R. E., & Geldart, L. P. (1982). *Exploration seismology*. Cambridge University Press.

785 Spikes, K. T., Tisato, N., Hess, T. E., & Holt, J. W. (2019). Comparison of geophone and  
786 surface-deployed distributed acoustic sensing seismic data. *Geophysics*.  
787 <https://doi.org/10.1190/geo2018-0528.1>

788 Steeples, D. W., Green, A. G., McEvilly, T. V., Miller, R. D., Doll, W. E., & Rector, J. W. (1997).  
789 A workshop examination of shallow seismic reflection surveying. *The Leading Edge*,  
790 16(11), 1641–1647. <https://doi.org/10.1190/1.1437543>

791 Steeples, D. W., & Miller, R. D. (1998). Avoiding pitfalls in shallow seismic reflection surveys.  
792 *GEOPHYSICS*, 63(4), 1213–1224. <https://doi.org/10.1190/1.1444422>

793 Truffer, M., Larsen, C., & Fahnestock, M. (2021). Basal conditions of Malaspina Glacier [Data  
794 set]. International Federation of Digital Seismograph  
795 Networks. [https://doi.org/10.7914/SN/3J\\_2021](https://doi.org/10.7914/SN/3J_2021)

796 Tsoflias, G. P., Ivanov, J., Anandakrishnan, S., & Miller, R. (2008). Use of Active Source  
797 Seismic Surface Waves in Glaciology. *Symposium on the Application of Geophysics to  
798 Engineering and Environmental Problems 2008*, 1240–1243.  
799 <https://doi.org/10.4133/1.2963234>

800 Uyanik, O. (2011). The porosity of saturated shallow sediments from seismic compressional and  
801 shear wave velocities. *Journal of Applied Geophysics*, 73(1), 16–24.  
802 <https://doi.org/10.1016/j.jappgeo.2010.11.001>

803 Wagner, F. M., Mollaret, C., Günther, T., Kemna, A., & Hauck, C. (2019). Quantitative imaging  
804 of water, ice and air in permafrost systems through petrophysical joint inversion of  
805 seismic refraction and electrical resistivity data. *Geophysical Journal International*,  
806 219(3), 1866–1875. <https://doi.org/10.1093/gji/ggz402>

807 Xie, Z., Komatitsch, D., Martin, R., & Matzen, R. (2014). Improved forward wave propagation  
808 and adjoint-based sensitivity kernel calculations using a numerically stable finite-element  
809 PML. *Geophysical Journal International*, 198(3), 1714–1747.  
810 <https://doi.org/10.1093/gji/ggu219>

811 Yang, Z. (Joey), Dutta, U., Xu, G., Hazirbaba, K., & Marx, E. E. (2011). Numerical analysis of  
812 permafrost effects on the seismic site response. *Soil Dynamics and Earthquake*  
813 *Engineering*, 31(3), 282–290. <https://doi.org/10.1016/j.soildyn.2010.08.004>

814 Yde, J. C., & Paasche, Ø. (2010). Reconstructing Climate Change: Not All Glaciers Suitable.  
815 *Eos, Transactions American Geophysical Union*, 91(21), 189–190.  
816 <https://doi.org/10.1029/2010EO210001>

817 Yilmaz, Ö. (2001). *Seismic Data Analysis: Processing, Inversion, and Interpretation of Seismic*  
818 *Data*. Society of Exploration Geophysicists. <https://doi.org/10.1190/1.9781560801580>